CK2 signaling from TOLLIP-dependent perinuclear endosomes is an essential feature of *KRAS* mutant cancers

Srikanta Basu[1], Brian T. Luke[2], Baktiar Karim[3], Nancy Martin[1], Stephen Lockett[4], Sudipto Das[5], Thorkell Andresson[5], Karen Saylor[6], Serguei Kozlov[7], Laura Bassel[7], Dominic Esposito[8], and Peter F. Johnson[1*]

[1]Mouse Cancer Genetics Program, Center for Cancer Research, National Cancer Institute, Frederick, Maryland, USA; [2]Advanced Biomedical Computational Science, Frederick National Laboratory for Cancer Research, Frederick, MD, USA; [3]Laboratory Animal Sciences Program, Frederick National Laboratory for Cancer Research, Frederick, MD, USA; [4]Optical Microscopy and Image Analysis Laboratory, Cancer Research Technology Program, Frederick National Laboratory for Cancer Research, Frederick, Maryland, USA; [5]Protein Characterization Laboratory, Cancer Research Technology Program, Leidos Biomedical Research, Inc., Frederick National Laboratory for Cancer Research, Frederick, Maryland, USA; [6]Laboratory Animal Sciences Program, Leidos Biomedical Research, Inc., Frederick National Laboratory for Cancer Research, Frederick, Maryland, USA; [7]Center for Advanced Preclinical Research, Frederick National Laboratory for Cancer Research, NCI, Frederick, Maryland, USA; [8]NCI RAS Initiative, Frederick National Laboratory for Cancer Research, Leidos Biomedical Research, Inc., Frederick, Maryland, USA

***corresponding author**

Abstract

Oncogenic RAS induces perinuclear translocation of the oncogenic kinases ERK1/2 and CK2 and the MAPK scaffold KSR1, forming endosomal signaling hubs termed perinuclear signaling centers (PSCs). PSCs are found in nearly all cancer cell lines and tumor tissues, suggesting that compartmentalization of oncogenic kinases drives tumorigenesis. We show here that the endosomal adaptor, TOLLIP, tethers RAB11A^{+} signaling endosomes containing CK2 and KSR1, but not ERK, to the perinuclear ER. TOLLIP binds to the KSR1 CA5 pseudo-kinase domain through a conserved region predicted to form a β-hairpin, thus anchoring PSCs to perinuclear endosomes. TOLLIP is perinuclear in cancer cells and *KRas*^{G12D}-driven mouse tumors but is pan-cytoplasmic in non-transformed cells, correlating with the presence of PSCs. TOLLIP is required for proliferation/survival of *KRAS* mutant tumor cells but not *HRAS, NRAS* and *BRAF* cancers or non-transformed cells. *KRas*^{G12D}-induced lung lesions in *Tollip*$^{KO/KO}$ mice showed reduced numbers of carcinomatous lesions, implicating TOLLIP in progression to malignant cancer. Phosphoproteomics studies revealed that perinuclear CK2 phosphorylates specific substrates, particularly proteins involved in ribosome biogenesis and translation such as RIOK1 and eIF4B. In summary, our findings identify TOLLIP as a key signaling adaptor in *KRAS* tumors whose inhibition is a potential vulnerability of these cancers.

Introduction

RAS proto-oncogenes are among the most frequently mutated in cancers, with ~19% of patients harboring *RAS* alterations[1]. Of the three *RAS* isoforms, *KRAS* is the most commonly mutated, representing 75% of all *RAS* mutant cancers, while *NRAS* (17%) and *HRAS* (7%) mutations occur less frequently. *KRAS* mutations are observed in 88%, 50% and 32% of pancreatic, colon and lung cancer patients, respectively, while *NRAS* alterations are predominantly associated with melanoma and *HRAS* mutations with thyroid and endometrial cancers[1,2]. RAS cancers are particularly aggressive and treatment-refractory[3,4], and mutant RAS typically triggers elevated, constitutive signaling through the RAF-MEK-ERK kinase cascade. Recent studies using integrative pharmacogenomics and phosphoproteomics have also demonstrated an essential role for the oncogenic kinase, CK2, in KRAS-driven lung and pancreatic adenocarcinomas[5-7]. Despite the importance of RAS effector kinases in tumorigenesis, drugs targeting effector kinases or RAS itself have met with limited success in producing effective therapeutic responses[8,9]. It is therefore important to explore additional features of oncogenic RAS signaling that may reveal novel targets for drug development.

A comprehensive molecular characterization of human lung adenocarcinomas (ADCs) revealed that p-ERK levels are moderate or low in a substantial proportion of tumor samples, including many that harbor *KRAS* mutations[10]. Similar findings were described for certain lung, colorectal, and pancreatic cancer cell lines[11-14] and endometrial cancer specimens[15]. RAS proteins actively signal from endosomes and other endo-membranes as well as the plasma membrane, and RAS signaling from endosomes stimulates downstream effector pathways that contribute to cellular transformation and tissue homeostatasis[16-22]. These findings suggest that features besides high MAPK pathway output contribute to RAS tumorigenesis. Consistent with this notion, we

showed that oncogenic RAS induces perinuclear re-localization of p-ERK, CK2 and the MAPK scaffold, KSR1[23]. These proteins form signaling hubs on nuclear-proximal endosomes termed perinuclear signaling centers (PSCs) whose formation is dependent on KSR1 and endosomal trafficking. PSC components CK2 and KSR1 colocalize with the recycling endosome (RE) marker, RAB11A, whereas p-ERK does not[18,23]. In serum-stimulated non-transformed cells, CK2 and p-ERK undergo delayed, transient perinuclear localization beginning at different times (4 and 6 h post-stimulation, respectively). These and other data demonstrate that p-ERK and CK2 are associated with distinct classes of endosomes.

We observed PSCs in all cancer cell lines tested and *KRas*^{G12D}-driven mouse lung tumors but not in non-transformed cells or normal lung tissue[23]. These observations suggest that PSC-associated effector kinases transmit oncogenic signals from active RAS, serving as critical signaling platforms in tumor cells. Therefore, we sought to elucidate the mechanisms that regulate perinuclear segregation of PSCs in tumor cells and to address whether PSC-associated kinases selectively access specific substrates. We show that TOLLIP, an endosomal adaptor and ubiquitin binding protein, directs CK2-containing endosomes to a perinuclear ER compartment but does not control ERK localization. TOLLIP was a specific dependency gene in tumor cells carrying mutant *KRAS* but not lesions in other *RAS* isoforms or *BRAF*. Tollip was also required for efficient progression of *KRas*^{G12V}-driven lung cancers to the adenocarcinoma stage, supporting its key role in malignant cancers. Finally, we identify a set of substrate proteins preferentially phosphorylated by perinuclear CK2. These findings underscore the importance of subcellular localization in signal transmission by oncogenic kinases.

Results

TOLLIP co-localizes with RAB11A$^+$, CK2-associated signaling endosomes in tumor cells. Endocytosis regulates the sorting, distribution, degradation and recycling of cargo proteins within cells, and modification of endosome trafficking in cancer cells is known to promote tumorigenesis[24,25]. It was reported that endosomes exist in two spatially distinct but dynamic pools: fast moving peripheral endosomes (PPE) and slow moving perinuclear endosomes (PNE)[26]. PNEs are tethered to the ER through association with the endosomal adaptor proteins EPS15, TOLLIP or TAX1BP1, which bind to mono-ubiquitinated SQSTM1 (p62) on ER membranes. We hypothesized that one or more of these adaptors may be involved in perinuclear targeting of signaling endosomes to form PSCs in tumor cells (Extended Data Fig. 1a).

As KSR1 interacts with multiple RAS effector proteins[27-29] and is required for PSC formation[23], we asked whether KSR1 binds to endosomal adaptors. Immunoprecipitation experiments in HEK293T cells showed that Pyo-tagged KSR1 interacted with endogenous TOLLIP and *vice versa* (Fig. 1a; Extended Data Fig. 1b). This association was not stimulated by oncogenic KRAS. Data mining from several published RNAi screens in tumor cell lines revealed that TOLLIP functioned as a dependency gene in three studies, two of which involved *KRAS* mutant cells[30-32]. These observations prompted us to further investigate the role of TOLLIP in oncogenic signaling.

Live cell imaging showed that EGFP-TOLLIP localized exclusively to the perinuclear region in A549 cells (human *KRAS*^{G12S} lung ADC), whereas it displayed diffuse pan-cytoplasmic distribution and a perinuclear component in non-transformed human bronchial epithelial (HBEC) cells (Fig. 1b). Nuclear proximity was quantified using an algorithm that measures the distance of

cytoplasmic signals from the nuclear envelope, normalized to a uniform distribution for the same cell. This relative nuclear proximity index (RNPI) showed an average $RNPI^{TOLLIP}$ of 0.4074 for A549 cells, and 0.6830 for HBEC cells ($p<0.0001$). Similar patterns were seen for endogenous TOLLIP (Extended Data Fig. 1c), mirroring the differential localization of KSR1, CK2α and p-ERK in A549 vs. HBEC cells, and for fluorescently-tagged KSR1 and CK2α in live cells (Extended Data Fig. 1d). Perinuclear compartmentalization of CK2α, p-ERK and TOLLIP was likewise apparent in PANC1 cells ($KRAS^{G12D}$ pancreatic ductal ADC) (Extended Data Fig. 1e). TOLLIP partially overlapped with KSR1 in A549 cells and displayed prominent co-occurrence with CK2α (Fig. 1c), which was especially evident from live cell imaging (Fig. 1d). However, TOLLIP showed minimal overlap with p-ERK. CK2α resides on perinuclear $RAB11A^{+}$ slow recycling endosomes in tumor cells[23]. Accordingly, IF (Fig. 1c) and live cell imaging (Fig. 1d) revealed abundant co-localization of TOLLIP with RAB11A, and RAB11A with CK2α and KSR1 (Extended Data Fig. 1f). The overlap of TOLLIP with CK2α, KSR1 and RAB11A but not p-ERK was confirmed using proximity ligation assays (Fig. 1e).

To test our prediction that PSCs occur on ER-tethered endosomes, we analyzed A549 cells co-expressing TOLLIP-mCherry and EGFP-tagged Sec61β, an ER marker. TOLLIP-positive endosomal vesicles were clearly embedded within the perinuclear ER network, and fluorescently tagged CK2α, KSR1 and RAB11A were also restricted to this region (Fig. 1f). Thus, perinuclear segregation of CK2 signaling endosomes in tumor cells involves their intimate association with the ER.

We previously observed juxtanuclear localization of KSR1, CK2 and p-ERK in $KRas^{G12D}$-driven mouse lung adenomas and ADCs but not in adjacent normal tissue[23]. Similarly, Tollip displayed intense perinuclear staining in lung ADCs but was pan-cytoplasmic in normal lung

epithelium (Extended Data Fig. 1g). Tollip was also perinuclear in pancreatic ductal adenocarcinomas (PDACs) arising in *LSL-Kras*^{G12D}/+;*p53*^{R172H}/+;*Pdx-Cre tg*/+ (*KPC*) mice (Extended Data Fig. 1h) and in orthotopic xenografts from a *KPC* PDAC-derived cell line but was diffusely cytoplasmic in normal pancreas (Extended Data Fig. 1i). Thus, the distinct subcellular partitioning of Tollip in cancerous vs. normal tissues recapitulates its distribution in cell lines.

TOLLIP is essential for perinuclear targeting of CK2 and proliferation of tumor cells. We used RNAi to elucidate the role of TOLLIP in PSC formation in tumor and non-transformed cells. TOLLIP silencing in A549 cells disrupted the perinuclear localization of KSR1, CK2α and RAB11A, leading to pan-cytoplasmic distribution of each protein, but did not significantly affect p-ERK (Fig. 2a; Extended Data Fig. 2a). Similar results were seen for PANC1 cells (Extended Data Fig. 2b). Thus, TOLLIP is required for perinuclear targeting of RAB11A^{+} endosomes containing CK2α and KSR1. TOLLIP silencing also severely diminished proliferation of A549 and PANC1 cells (Fig. 2b) and two other *KRAS* mutant cell lines, MIA-Paca-2 (PDAC) and MDA-MB-231 (breast cancer) (Extended Data Fig. 2c). The growth defect in A549 cells was associated with increased senescence and apoptosis (Fig. 2c). By contrast, TOLLIP ablation had little effect on proliferation of HBEC cells (Fig. 2d) or MEFs (Extended Data Fig. 2d), where *Tollip*$^{KO/KO}$ cells grew similarly to *WT* controls.

As TOLLIP, KSR1 and CK2α are associated with RAB11A^{+} endosomes, we investigated whether RAB11A is required for their perinuclear localization. All three proteins became pan-cytoplasmic upon RAB11A silencing (Fig. 2e,f). RAB11A depletion also impaired A549 cell proliferation (Extended Data Fig. 2e). Conversely, TOLLIP localization was unaffected by KSR1 depletion (Extended Data Fig. 2f), although loss of KSR1 disrupts CK2 PSCs[23]. These data suggest

that TOLLIP dependency in tumor cells involves its ability to target CK2 signaling endosomes to the ER and support a model in which KSR1 connects CK2 to perinuclear RAB11A$^+$ endosomes by binding to TOLLIP, which tethers these vesicles to the ER.

A highly conserved sequence in TOLLIP interacts with the KSR1 CA5 domain. Since KSR1-TOLLIP binding appears to recruit signaling complexes to perinuclear endosomes, we sought to further characterize this interaction. We generated a nested set of Pyo-tagged KSR1 C-terminal deletion mutants with endpoints at the N-terminal boundaries of five conserved areas (CA1-5; Extended Data Fig. 3a)[33], which correspond to known functional domains. CA1 is specific to KSR1 and binds CK2[29], CA3 has similarity to atypical C1 lipid binding domains[34], CA4 binds ERK[35], and CA5 is a pseudokinase domain homologous to RAF kinases that interacts with MEK[27,28,36] and RAF[37]. Co-IP analysis of Pyo-KSR1 deletion mutants expressed with rat HA-Tollip in HEK293T cells showed that removal of CA5 (CA1-4) abolished the KSR1-Tollip interaction (Extended Data Fig. 3a). Interestingly, further deletion of CA4 (CA1-3) partially restored Tollip binding, while loss of CA3 (CA1-2) eliminated this interaction altogether. A protein consisting of CA5 alone also bound Tollip efficiently. Thus, KSR1 CA5 appears to be the major site of Tollip interaction. CA3 is also capable of binding Tollip, but this association is inhibited by the CA4 region.

TOLLIP is composed of three main functional domains: TBD (Tom1 binding domain), C2 (phosphatidylinositol binding domain) and CUE (ubiquitin binding domain)[38-41] (Fig. 3a). We expressed Pyo-KSR1 with HA-tagged WT Tollip or various deletion mutants[38] and performed co-IP assays (Fig. 3a; Extended Data Fig. 3b). WT Tollip and Δ229-274 (lacking CUE) bound KSR1 efficiently. However, Δ180-274 did not, indicating that the "linker" region between C2 and CUE

(residues 179-229) is required for this association. The 179-229 sequence displays marked evolutionary preservation among vertebrate species (Fig. 3b), particularly an 18 aa core (185-202) that is nearly perfectly conserved. Δ203-274, which adds residues 179-202 to Δ180-274, restored the Tollip:KSR1 interaction. A Tollip mutant lacking only residues 180-202 (Δ180-202) lost nearly all KSR1 binding activity. Thus, the invariant sequence between C2 and CUE is essential for the association with KSR1. A predicted human TOLLIP structure generated by the neural network-based modelling tool, AlphaFold2.0[42], shows a β-hairpin fold corresponding to the conserved 185-202 region (Fig. 3c). The β-hairpin feature is absent in the model for *C. elegans* Tollip, which lacks this sequence. Although the β-hairpin fold has a low confidence score, its precise alignment with the 185-202 motif implies that this structure plays a key role in KSR1 binding.

***Tollip* is a dependency gene specific to KRAS-driven cancers.** Because loss of TOLLIP is toxic to *KRAS* mutant tumor cells (Fig. 2), we asked if TOLLIP dependency is specific to *KRAS*-transformed cells. We first depleted Tollip in NIH3T3 cells expressing $KRAS^{G12V}$ or $HRAS^{G12V}$ and assessed CK2α and KSR1 localization. Both *RAS* oncogenes induced perinuclear translocation of CK2α, KSR1 and Tollip in shCtrl cells (Fig. 4a; Extended Data Fig. 4a). However, Tollip depletion elicited pan-cytoplasmic redistribution of CK2α and KSR1 in $NIH3T3^{KRAS}$ cells but had little effect on $HRAS^{G12V}$-transformed cells (Fig. 4a). The disruption of PSCs correlated with reduced proliferation, as Tollip depletion decreased the growth rate of $NIH3T3^{KRAS}$ cells (Fig. 4b) but did not appreciably affect $NIH3T3^{HRAS}$ cells (Fig. 4c). The slower proliferation rate of non-transformed NIH3T3 cells was unaffected by Tollip silencing (Fig. 4b,c). The KRAS vs. HRAS effect was also seen in $Tollip^{-/-}$ MEFs, which carried an immortalizing $p19^{ARF}$ null mutation to permit transformation by oncogenic *RAS* (Extended Data Fig. 4b,c). The proliferation of *KRAS*-

expressing *Tollip*$^{-/-}$ cells was reduced to that of non-transformed cells. Thus, *KRAS*-driven PSC formation and increased proliferation requires Tollip, while transformation by *HRAS* is Tollip-independent.

We also depleted TOLLIP in a panel of human tumor cell lines harboring various *RAS* pathway oncogenes. Growth of *HRAS* mutant T24 bladder carcinoma cells was relatively unaffected by TOLLIP silencing, and CK2α and KSR1 remained fully perinuclear (Fig. 4d,e). *KRAS*-transformed A549 cells displayed reduced clonogenic growth in the absence of TOLLIP (Extended Data Fig. 4d), whereas *NRAS* mutant H1299 cells (lung ADC), *BRAF*^{V600E}-driven A375 melanoma cells and *PTEN/TP53* null PC3 prostate cancer cells were only minimally affected by loss of TOLLIP (Extended Data Fig. 4d). Thus, of the tumor cell lines tested, those without *KRAS* mutations are resistant to TOLLIP deficiency. Since PSCs are induced by oncogenic *HRAS* in NIH3T3 cells and are present in human tumor cells that carry oncogenes other than *KRAS*, another endosomal adaptor(s) likely provides a redundant function in these cells.

Tollip facilitates progression to adenocarcinoma in a *Kras*^{G12D}-driven model of lung cancer. To investigate whether Tollip deficiency impairs *Kras*-induced tumor development *in vivo*, we generated *Tollip*$^{-/-}$ mice[41] carrying the Cre-activated *LSL-Kras*^{G12D} oncogene[42]. Ad.Cre virus was administered to the lungs of *LSL-Kras*^{G12D};*Tollip*$^{+/+}$ and *Tollip*$^{-/-}$ mice to initiate tumorigenesis, and animals were monitored until disease severity required euthanasia. All mice eventually succumbed to respiratory distress due to accumulated pulmonary lesions. No survival difference was observed between genotypes (Log-rank test; $p = 0.96$) (Fig. 5a). Lung lesions in this model are primarily benign alveolar hyperplasia and adenomas, a few of which advance to malignant adenocarcinoma (ADC) (Fig. 5b). To further characterize lung lesions, we used an AI-based

algorithm (HALO image analysis software; Indica Labs) to evaluate H&E slides. Areas of hyperplasia and overall tumor burdens (representing all lesion grades beyond hyperplasia) were similar between the two genotypes (Fig. 5c). Benign adenomas versus atypical adenomas and carcinomas were not reliably classified by the AI algorithm and were assessed by standard pathological evaluation. This analysis showed that carcinomatous lesions were the highest grade observed in 88.2% of *Tollip*$^{+/+}$ mice, whereas only 35.3% of *Tollip*$^{-/-}$ animals presented with ADCs (p=0.0039; Fisher's exact test) (Fig. 5d). These findings demonstrate a significant block to *Kras*-driven ADC development in mutant animals and are consistent with an important role for Tollip in malignant lung cancer.

The mouse tumor experiment used a germline *Tollip* mutation. To address whether the phenotype involves tumor cell-intrinsic loss of Tollip, we tested the tumorigenicity of TOLLIP-depleted A549 cells by tail vein injection into immune-deficient mice (Fig. 5e). Cells expressing a control shRNA formed an average of 60 lung lesions per animal. However, two different shTOLLIP constructs almost completely prevented tumor formation, with most recipient mice displaying no detectable lesions. Thus, human lung ADCs are highly dependent on TOLLIP for tumor engraftment.

Phosphoproteomics analysis to identify targets of perinuclear kinases. The presence of oncogenic kinases on perinuclear endosomes in tumor cells suggests that they access a unique set of targets to promote neoplastic transformation. To identify phospho-sites that correspond with PSCs, we carried out three different kinds of phosphoproteomic experiments. We first used serum-stimulated NIH3T3 cells to exploit the temporal features of growth factor (GF)-induced PSC formation, where CK2α becomes perinuclear at 4 and 6 h and p-ERK re-localizes at 6 h[23] (Fig.

6a). We performed phosphoproteome profiling of NIH3T3 cell lysates harvested at 0, 0.5, 2, 4, 6 and 8 h post-stimulation. After protease digestion and isobaric labeling, phosphopeptides (p-peptides) were isolated by TiO_2 enrichment and subjected to LC-MS/MS p-peptide mapping. The TiO_2 flow-through was used to determine total protein abundance, from which normalized p-peptide values were calculated.

To isolate phosphorylation events that track PSC formation, we filtered the data for p-peptides that increased by ≥1.5-fold at 4 and/or 6 h relative to unstimulated (0 h) cells and also showed an increment of ≥1.2-fold versus 0.5 and 2 h. P-peptides that passed these tests in at least 2 of 3 replicates were subjected to further analysis. 76 p-peptides were observed at 4 h and 143 sites at 6 h, and 29 of these were common to both 4 and 6 h (Fig. 6b). P-peptides were then analyzed for the presence of known modification sites and/or similarity to consensus phosphorylation motifs. Predicted CK2 sites matching the consensus motif pS/pT•X•X•D/E[43] were highly represented across all p-peptides (53% of sites in all time points combined), possibly reflecting the large number of reported CK2 phosphorylation sites[44]. IPA network analysis of all p-peptides in the 4, 6 and 4+6 h samples revealed CK2 kinase nodes (Extended Data Fig. 5a). Putative CK2 sites were modestly enriched in p-peptides up-regulated at 4 h (57%), 6 h (57%) and 4+6 h (55%) (Fig. 6b). Thus, some of these sites may represent PSC-dependent phosphorylation events.

Of the 16 CK2 site-containing p-peptides up-related at 4+6 h, 7 are known CK2 sites either reported from studies of individual proteins or in phosphoproteomic data sets (Fig. 6c). Gene ontology analysis (molecular function) of these proteins revealed poly(A) RNA binding and translation initiation factor activity as significantly enriched categories (Fig. 6d); proteins related to translation include Eif4b, Eif5b, Pdcd4, and Riok1. The 4 h and 6 h sets (CK2 p-peptides only) also showed poly(A) RNA binding as the top GO term (Fig. 6e,f), and all three sets included

translation initiation as an enriched biological process (Extended Data Fig. 5b). These results suggest that perinuclear CK2 signaling endosomes formed during late G1 phase phosphorylate proteins that regulate translation and RNA metabolism, as well as transcription and chromatin.

As a complementary approach, we identified TOLLIP-dependent modifications by comparing phosphoproteomes in control and TOLLIP-depleted A549 cells and in $KRAS^{G12V}$-expressing $p19^{Arf-/-}$ and $p19^{Arf-/-};Tollip^{-/-}$ MEFs. TOLLIP was silenced in A549 cells using three independent shRNAs compared to a control shRNA, and p-peptides were characterized by LC-MS/MS. Ratios of normalized p-peptide intensities in control vs. TOLLIP knockdown cells were calculated and those that were significantly higher in control cells (90% CI) defined a list of TOLLIP-dependent sites. The corresponding proteins were associated with a CK2 kinase node (IPA network analysis; Extended Data Fig. 5c). Filtering for CK2 sites generated a final set of 15 p-peptides (Fig. 6g). Analysis of these proteins for molecular function and biological processes again showed poly(A) RNA binding as a top-ranked category (Fig. 6h and Extended Data Fig. 5d).

To analyze *Tollip* KO MEFs, cells were transduced with $KRAS^{G12V}$ or control lentiviruses and phosphoproteomic analysis was performed (Extended Data Fig. 5e). Ratios of normalized p-peptide intensities in *KRAS* versus control cells were calculated, and those that increased significantly (90% CI) in $Tollip^{+/+}$ cells were used to define a *KRAS*-induced phosphoproteome (89 p-peptides). The fold change (FC) of these p-peptides was then divided by the corresponding FC in $Tollip^{-/-}$ cells to produce $Tollip^{+/+}$:$Tollip^{-/-}$ FC ratios. All 89 p-peptides displayed FC ratios >1.5 and thus were defined as Tollip-dependent modifications. Twenty-seven of these were phosphorylated on predicted CK2 sites (Fig. 6i). GO analysis of these proteins revealed enrichment for genes involved in cell-cell adhesion and poly (A) RNA binding (Fig. 6j; Extended Data Fig. 5g).

Two common CK2 site phospho-sites, corresponding to eIF4B (translation initiation) and TPD52L2 (membrane trafficking), were shared in at least 2 of the 3 screens (Fig. 6k). In addition, 7 common proteins were observed (≥ 2/3 screens), of which 5 were phosphorylated on different CK2 sites (Fig. 6l). The 7 proteins were enriched for poly (A) RNA binding and poly (A) tail shortening functions (Fig. 6l; Extended Data Fig. 5h). These overlaps are likely to be a significant underestimate of common CK2 PSC-dependent substrates; for example, RIOK1 was not present by MS analysis in MEFs or A549 cells but was readily detected by immunoblotting (see below).

Phosphorylation of the atypical kinase RIOK1 by perinuclear CK2 controls its pro-oncogenic activity. One of the proteins identified as a likely perinuclear CK2 substrate is the non-canonical protein kinase, RIOK1. RIOK1 was phosphorylated on a predicted CK2 site, $pS^{21}pS^{22}$DSE, at 4 and 6 h in GF-stimulated NIH3T3 cells, although the protein was not detected in MEFs and A549 cells. RIOK1 is required for processing of 18S-E pre-rRNA to the mature 18S rRNA[45] and for assembly/maturation of the 40S ribosomal subunit[46,47] and thus has a central role in protein synthesis. RIOK1 was also identified as a synthetic lethal gene in *KRAS* mutant cancers[48] and is essential for viability of various tumor cell lines[49] and cancers[50]. Moreover, CK2 has been implicated as a RIOK1 Ser21/22 kinase[51] and this site is conserved among mammalian RIOK1 homologs (Fig. 7a). We therefore investigated whether Ser21/22 phosphorylation is a functionally important modification catalyzed by perinuclear CK2 in tumor cells.

We used a phospho-CK2 site antibody reagent that recognizes many pS/pT•X•X•D/E motifs to analyze RIOK1 phosphorylation. Flag-tagged *WT* RIOK1 or S21A/S22A mutants were expressed in 293T cells without or with $KRAS^{G12V}$. Following Flag immunoprecipitation, samples were analyzed by immunoblotting with p-CK2 substrate or Flag antibodies (Fig. 7b). p-RIOK1

levels increased when $KRAS^{G12V}$ was co-expressed, while the S21/22A mutation decreased but did not eliminate phosphorylation. Thus, multiple CK2 sites on RIOK1 are inducibly phosphorylated, of which S21/S22 is a major phosphoacceptor. When the same experiment was performed in TOLLIP depleted cells, total p-RIOK1 and p-S21/S22-specific CK2 site signals were reduced, consistent with phosphorylation requiring TOLLIP-dependent perinuclear CK2 endosomes. We next tested the ability of RIOK1 S21/S22 mutants to rescue RIOK1-depleted cells. We confirmed that A549 cells are highly dependent on RIOK1 for clonogenic growth (Fig. 7c). Expression of exogenous WT RIOK1 partially restored colony formation, while S21/22A did not (Fig. 7d). A potential phosphomimetic mutant, S21/22D, also did not complement RIOK1 knockdown, which could indicate that the phosphorylated residue(s) contribute to a protein interaction surface that is not mimicked by a negatively charged amino acid.

RIOK1 regulation of 18S-E pre-rRNA processing can be monitored by analyzing levels of the 5' internal transcribed spacer 1 (ITS1) in the precursor RNA by RNA FISH. When processing is impaired, the precursor accumulates in the cytoplasm[47]. We confirmed that RIOK1 depletion in A549 cells increased cytoplasmic 5'ITS1 FISH signals (Fig. 7e). To determine whether TOLLIP is also involved in this RIOK1-dependent step, we performed the same analysis in TOLLIP knockdown cells. Cytoplasmic 5'ITS1 signals were increased by a similar amount when TOLLIP was depleted. These data support a pathway whereby TOLLIP-dependent, CK2-mediated phosphorylation of RIOK1 is necessary for RIOK1 to facilitate 18S rRNA processing and 40S ribosome maturation.

Discussion

Receptors, kinases, scaffold proteins and RAS proteins can be internalized and signal from endomembranes[52]. However, the functional consequences of this subcellular compartmentalization, such as whether it affects the substrate selectivity of kinases, are unclear. There is also scant information on whether compartmentalized signaling differs in transformed and normal cells. Our study shows that oncogenic RAS induces the association of signaling endosomes with the perinuclear ER network. PSCs involving CK2 and KSR1, but not ERK1/2, require the endosomal adaptor TOLLIP for spatial partitioning to the perinuclear region. TOLLIP was originally identified as a negative regulator of pro-inflammatory signaling[39] but has not been linked to the RAS pathway in tumor cells. TOLLIP co-localizes with CK2α and KSR1 on perinuclear RAB11A$^+$ endosomes, and TOLLIP ablation causes their redistribution throughout the cytoplasm. This pattern in TOLLIP-depleted tumor cells is similar to that of non-transformed cells, indicating that TOLLIP-mediated perinuclear targeting of CK2 signaling endosomes is a key feature of oncogenic signaling.

Our findings indicate that TOLLIP recruits KSR1:CK2 complexes[29] to a specific class of RAB11A$^+$ signaling endosomes. The mechanism involves TOLLIP binding to KSR1 through a short, conserved region adjacent to the CUE ubiquitin-binding domain. Although the function of this "linker" region was previously unknown, it was recently shown to mediate the association of TOLLIP with STING (stimulator of interferon genes), stabilizing STING and maintaining cGAS-STING signaling in response to microbial pathogens[53]. Our work adds to the increasing evidence that TOLLIP is involved in a variety of signaling pathways[54,55] besides its original role in suppressing TLR and IL-1 receptor signaling during the resting state[56,57]. Whether the effect of TOLLIP on inflammatory signaling is distinct from its role in perinuclear targeting of RAS effector signaling complexes remains to be determined.

Jongsma et al.[26] identified three adaptor proteins, including TOLLIP, as ubiquitin binding proteins that tether endosomes to the ER. TOLLIP mainly targeted CD63-positive late endosomes for ER attachment. Our work extends these findings by showing that in tumor cells, TOLLIP is primarily found on RAB11A$^+$ endosomes containing KSR1 and CK2. The endosome-ER tethering function of TOLLIP is critical for oncogenic signaling in *KRAS* tumor cells. However, it is not essential in normal cells, where PSCs only form transiently in response to GFs and cell proliferation and viability is largely unaffected by TOLLIP depletion. The mechanism underlying the selective perinuclear attachment of signaling endosomes in transformed versus normal cells and whether and how TOLLIP association with endosomes is regulated by dysregulated RAS signaling are important questions for future study.

KRAS-transformed cells are selectively dependent on TOLLIP to tether CK2 signaling endosomes to the perinuclear ER and for efficient proliferation/survival. In contrast, tumor cells with mutations in *HRAS*, *NRAS* or *BRAF* also display perinuclear CK2 and KSR1 but are largely unaffected by TOLLIP depletion. We infer that there are alternative pathways for PSC formation involving different endosomal adaptors. Adding further complexity to this picture, ERK1/2 kinases are associated with a unique class of signaling endosomes that lack TOLLIP, and ERK remains perinuclear in TOLLIP-deficient cells. It will be of considerable interest to identify other endosomal adaptors that establish the complete signaling landscape in tumor cells and to elucidate those that act redundantly to TOLLIP in cells transformed by other *RAS* pathway oncogenes.

We suggest that PSCs act as critical signaling engines that drive neoplastic transformation and cancer and this involves selective phosphorylation of proteins required to meet the demands of rapid cell proliferation, altered metabolism and other features of tumor cells. Phosphoproteomics experiments in three different systems identified a set of targets whose

phosphorylation is associated with TOLLIP-dependent, perinuclear compartmentalization of CK2 (Fig. 6; Extended Data Fig. 5). These proteins are enriched for biological functions such as translation initiation (eIF5A, eIF4B), ribosome biogenesis (RIOK1), and poly(A) RNA binding, which is also related to translation[58,59]. The CK2 site in RIOK1 (Ser21/22) was critical for RIOK to support proliferation/survival of A549 cells. The final step of pre-18S rRNA processing, which is dependent on RIOK1, also required TOLLIP, further supporting a model in which ER-tethered CK2 signaling endosomes control phosphorylation of key targets in tumor cells.

Tollip facilitates the development of *Kras*^{G12D}-driven lung ADCs but is dispensable for benign lesions such as neoplasia and adenomas. Progression to carcinoma in *Kras* lung cancer models has been linked to increased MEK-ERK signaling, as evidenced by high p-ERK levels that are often associated with amplification of the mutant *Kras* locus[60]. Interestingly, *Kras*-induced adenomas display perinuclear CK2 and KSR1[23], as well as Tollip (Extended Data Fig. 1g), even though these lesions form in the absence of Tollip. Evidently there is a transition accompanying progression to ADC that results in Tollip dependency, which may involve increased flux through the RAS pathway. Human *KRAS* mutant cell lines are nearly always derived from these late-stage malignant cancers, which likely explains their requirement for TOLLIP. TOLLIP addiction may represent an Achilles heel of *KRAS* cancers and a potential target for anti-cancer therapeutics.

Acknowledgements

We thank Dr. A. Ciarrocchi for providing *Tollip* constructs, T.N. O'Sullivan for technical assistance in generating KPC pancreatic tumor samples and A. Kane (Scientific Publications, Graphics & Media, Leidos Biomedical Research, Inc., Frederick National Laboratory for Cancer Research) for preparation of figures. This research was supported in part by the Intramural

Research Program of the NIH, National Cancer Institute, Center for Cancer Research, and in part with Federal funds from the National Cancer Institute, National Institutes of Health, under Contract No. HHSN261200800001E. Analysis and management of images and associated metadata was supported in part by the NCI HALO Image Analysis Resource. The content of this publication does not necessarily reflect the views or policies of the Department of Health and Human Services, nor does mention of trade names, commercial products, or organizations imply endorsement by the U.S. Government.

Methods

Animal experiments. Mice were maintained in accordance with NIH animal guidelines following protocols approved by the NCI-Frederick Animal Care and Use Committee. Mouse embryonic fibroblasts (MEFs) were isolated from *WT*, *Tollip*$^{-/-}$[57], *p19*$^{Arf-/-}$ and *p19*$^{Arf-/-}$*;Tollip*$^{-/-}$ E13.5 mouse embryos (C57Bl/6Ncr strain background), and cells were maintained at low passage. *Kras*^{LA2}/+[61], *LSL-Kras*^{G12D}/+[62] and *Tollip*$^{-/-}$*;LSL-Kras*^{G12D}/+ mice (C57Bl/6Ncr background) were used for animal studies. To induce lung tumors in *LSL-Kras*^{G12D} strains, Ad.Cre virus (Viral Vector Core Facility, University of Iowa College of Medicine) was administered by intratracheal instillation at a dose of 1.5 or 3.0x10^{7} pfu/animal. Animals that became moribund (thin, hunched, labored breathing, rough coat, or lethargy) were sacrificed, lungs were removed and fixed in 10% Neutral Buffered Formalin (NBF) and embedded in paraffin blocks. Lungs from normal mice were used as controls. NBF fixed paraffin-embedded pancreatic tumor tissue sections were obtained from KPC mice (*Pdx-1-Cre (B6.Tg(Pdx1-cre)6Tuv/Nci)*; *LSL-Kras*^{G12D} (*B6.Krastm4Tyj/Nci*); *LSL p53*^{R172H} *(129S4-Trp53tm2Tyj/Nci)* on a C57BL/6 background)[63]. Pancreas samples from *WT* mice were used as controls. Primary tumor cell line KPC98027 was derived from a KPC pancreatic

ductal adenocarcinoma. $1x10^5$ KPC cells were injected into medial pancreata in syngeneic C57BL/6 recipient animals. Pancreas from un-injected normal mice were used as controls. Tumors were collected at 5-6 weeks post-injection and fixed in NBF as described above. For xenograft experiments, athymic nude (*nu/nu*) mice received 1×10^6 A549 cells (control or TOLLIP knockdown) by tail vein injection. All mice were sacrificed when a single mouse showed clinical signs and became moribund. Lungs were removed and lesions counted. Lungs were gently inflated in NBF, fixed with NBF for 5 days and embedded in paraffin blocks or stored in 70% ETOH.

H&E staining, tumor grading and HALO AI-based image analysis of lung tumor slides. Mouse lungs were formalin-fixed, embedded in paraffin and sectioned at 5µm thickness. Routine hematoxylin and eosin-staining was performed using the Sakura® Tissue-Tek® Prisma™ automated stainer (Sakura Finetek USA, Inc., Torrance, California). The slides were dewaxed using xylene and then hydrated using a series of graded ethyl alcohols. Commercial hematoxylin, clarifier, bluing reagent and eosin-Y were used to stain. A regressive staining method was used, which intentionally overstains tissues and then uses a differentiation step (clarifier/bluing reagents) to remove excess stain. After staining was completed, the slides were cover slipped using the Sakura® Tissue-Tek™Glass® automatic cover slipper (Sakura Finetek USA, Inc., Torrance, California). Whole slide images were obtained at high resolution, 20x magnification using an AT2 scanner (Aperio, Leica Biosystems, Buffalo Grove, IL, USA).

Two veterinary pathologists (B.K. and L.B.) identified and segmented the regions of interest used to train an AI deep learning tissue-classifying algorithm (Densenet AI V2 plugin in Halo (v.3.3.2541.423, Indica Labs, Corrales, NM, USA). Annotations were manually drawn around four tissue classes: normal (including lung parenchyma, airways and vessels), hyperplasia

(hypercellular foci of round to cuboidal hypertrophic pneumocytes arranged in a single layer), adenoma (expansile mass consisting of proliferative epithelium arranged in papillary to solid formations with no features of atypia and rare to absent mitotic figures), and atypical foci (proliferative cells demonstrating some combination of increased cellular atypia, anisocytosis, anisokaryosis, cytoplasmic basophilia, increased mitotic figures and haphazard or invasive patterns [carcinoma]).

During training, the algorithm performance was iteratively evaluated by visual inspection and misclassification of tissues was addressed and corrected by the addition of additional annotations in the misclassified regions and additional training until satisfactory performance was obtained. During validation it was demonstrated that the AI module could not consistently differentiate adenomas from adenocarcinomas or atypical foci as determined by the pathologists and these classes were grouped together for subsequent analysis. The percentages of lungs comprised of hyperplasia and adenoma (including regions of cellular atypia and pleomorphism) were calculated by dividing the absolute value of each class by the total tissue area on the slide and multiplying by 100.

Cells and cell culture. HEK-293T cells (American Type Culture Collection (ATCC), Rockville, MD) and MEFs were cultured in DMEM+Glutamax (supplemented with 10% Fetal Bovine Serum (FBS). HBEC cells (ATCC) were cultured in Airway Epithelial Cell Basal Medium (ATCC® PCS-300-030) supplemented with Bronchial Epithelial Cell Growth Kit (ATCC PCS-300-040). NIH3T3 cells were grown in DMEM+Glutamax with 10% calf serum (Colorado Serum Company). A549 (ATCC) cells were grown in Ham's F-12K (Kaighn's) medium with 10% FBS. PANC-1, A-375, MDA-MB-231, and MIA PaCa-2 cells (ATCC) were grown in

DMEM+Glutamax with 10% FBS. PC-3 and NCI-H1299 cells (ATCC) were grown in RPMI+Glutamax with 10%FBS. KPC98027 cells were cultured in DMEM/F12+Glutamax with 10% FBS. *HRAS* mutant cancer cell lines T24 and RL95-2 were kindly provided by Dr. Deborah Morrison (NCI-Frederick) and were grown in McCoy's 5A (modified) and DMEM/F12+Glutamax, respectively. All media and FBS were obtained from Thermo Fisher Scientific. To prevent Mycoplasma contamination, cell cultures were additionally supplemented with Plasmocin (InvivoGen). Cell stocks were generally passaged fewer than 5 times, and freshly thawed cells were maintained in culture for no more than 2 weeks before conducting experiments.

Antibodies and reagents. Rabbit polyclonal antibodies to TOLLIP (11315-1-AP) and RAB11A (20229-1-AP) were obtained from Proteintech Group. Mouse monoclonal antibody to Tollip (Clone: MAB4678) was obtained from R&D Systems. Rabbit Anti-CSNK2A1 (CK2a) antibody (ab10466) was from Abcam. Rabbit antibodies to phospho-ERK1/2 (#9101), HA-Tag (#3724) and Phospho-CK2 Substrate [(pS/pT)DXE] MultiMab™ Rabbit mAb mix (#8738) were from Cell Signaling Technologies. Mouse antibody to β-Actin (sc-47778) and p-ERK1/2 (sc-136521) were obtained from Santa Cruz Biotechnology. Rabbit antibodies to HRAS (GTX-116041) and to KSR1 (GTX56241) were from GeneTex. Affinity purified mouse antibody against Pyo epitope tag (Glu-Glu) was from BioLegend (#901802). Mouse monoclonal antibody against KRAS (H00003845-M01) was obtained from Abnova. Anti-mouse (W4028) and anti-rabbit (W4018) HRP conjugated secondary antibodies were from Promega. Anti-mouse Alexa® Fluor 488 (#A32790) and anti-rabbit Alexa® Fluor 594 (A-21207) conjugated secondary antibodies were from Thermo Fisher Scientific.

Plasmids and lentiviral vectors. *Ksr1* expression plasmids containing an N-terminal Pyo tag (EYMPME) were generated by PCR amplification using pcDNA3 mouse *Ksr1*[64] as a template and inserting fragments into pcDNA3.1. C-terminal deletion mutants 1-81 (CA1), 1-286 (CA1-2) were cloned using EcoRI and BamH1 sites, while 1-377 (CA1-3), and 1-479 (CA1-4) were cloned using EcoR1 and Kpn1 restriction sites. N-terminal deletion mutant 531-873 (CA5) was inserted using EcoR1 and BamH1 sites. Expression plasmids for HA-tagged WT rat *Tollip* and deletion mutants (Δ229-274, Δ180-274, Δ1-54 and Δ1-94) in pRK7[38] were a kind gift from Dr. A. Ciarrocchi (Laboratory of Translational Research, Azienda Unità Sanitaria Locale-IRCCS di Reggio Emilia, Italy). HA-*Tollip* deletion mutant Δ203-274 was made by PCR amplification and cloning into the pRK7 vector using BamH1 and EcoR1 restriction sites. Δ180-202 was made using three-way ligation of cDNA fragments encoding *Tollip* residues 1-179 and 203-274, and BamH1/EcoR1 digested pRK7 vector; Nhe1 sites were used to join the two *Tollip* cDNA fragments. pLenti CMV GFP Hygro (656-4) was a gift from Eric Campeau and Paul Kaufman (Addgene plasmid #17446; http://n2t.net/addgene:17446; RRID:Addgene_17446)[65]. Human *TOLLIP* was amplified from cDNA isolated from A549 cells using primers containing BsrG1 and Sal1 sites and the product inserted into pLenti CMV GFP hygro vector. A BsrG1 site within the *TOLLIP* cDNA was eliminated by mutation using the QuikChange Lightning Site-Directed Mutagenesis Kit (Agilent, Catalog #210518) as per the manufacturer's instructions. Lentiviral expression vectors for GFP- or mCherry-tagged human *KSR1*, mCherry-tagged mouse *Ck2α*, and FLAG-tagged human *RIOK1* were obtained from Genecopoeia (Rockville, MD). The *RIOK1* Ser22 to Ala mutant and Ser21/22 to Ala double mutant were generated using QuikChange Lightning Site-Directed Mutagenesis Kit (Agilent, Catalog #210518). Primers were designed using the QuikChange Primer Design website. Lentiviral vectors for human $HRAS^{G12V}$ and $KRAS^{G12V}$ were obtained from the RAS Initiative (NCI

Frederick, NIH). Lentiviral packaging/envelope plasmids pMD2.G (#12259), pMDLg/pRRE (#12251), and pRSV/Rev (#12253) were obtained from AddGene. pLV-ER GFP encoding GFP tagged *SEC61β* was a gift from Pantelis Tsoulfas (Addgene plasmid #80069; http://n2t.net/addgene:80069; RRID:Addgene_80069), mEmerald-Rab11a-7 was a gift from Michael Davidson (Addgene plasmid #54245; http://n2t.net/addgene:54245; RRID:Addgene_54245). pTag-RFP-C-h-Rab11a-c-Myc was a gift from James Johnson (Addgene plasmid #79806; http://n2t.net/addgene:79806; RRID: Addgene_79806)[66]. The lentiviral pUltra-hot vector was a gift from Malcolm Moore (Addgene plasmid #24130; http://n2t.net/addgene:24130; RRID: Addgene_24130). mEmerald tagged human *RAB11A* and RFP tagged human *RAB11A* were cloned into the Ultra-hot vector using Age1 and BamH1 cloning sites. Similarly, mCherry tagged human *TOLLIP* was cloned into the Ultra-hot vector. Mission shRNA lentiviral constructs for human *TOLLIP* (TRCN0000314717 and TRCN0000356024 TRCN0000314642), mouse *Tollip* (TRCN0000066136 and TRCN0000066137) and human *RIOK1* (TRCN0000295923 and TRCN0000037399) were obtained from Millipore Sigma.

Transient transfection. Transfections were carried out using FuGENE 6 transfection reagent (Promega #E2691) per the manufacturer's instructions. Briefly, HEK293T cells in 100mm dishes were transfected with varying amounts of Pyo tagged *Ksr1* or deletion mutants (standardized to obtain equivalent protein expression), HA-tagged *Tollip* or *Tollip* deletion mutants (standardized to obtain equivalent protein expression), 2µg of FLAG tagged human *RIOK1 or RIOK1* mutants, with or without 0.1µg pcDNA3-$KRAS^{G12V}$. Empty pcDNA3 was added when necessary to equalize total vector DNA. 2µl FuGENE 6 transfection reagent per µg of DNA was used for each transfection. Transfection mix was made in antibiotic free Opti-MEM medium (Thermo Fisher

Scientific, Catalog #11058021). After transfection, cells were cultured in complete media (DMEM with 10% FBS) for 24 h. Media was changed and cells were incubated for another 24 h before harvesting. For experiments involving $KRAS^{G12V}$, media was changed 24 h after transfection and cells were incubated for 12 h in complete media followed by overnight incubation in low serum conditions (DMEM with 0.1% FBS) prior to harvesting.

Lentiviral infection. Lentiviral plasmids were transfected into 293T packaging cell lines, using a standard CaPO4 precipitation method. For lentivirus production, 20 µg lentiviral vector, 6 µg pMD2.G, 10 µg pMDLg/pRRE and 5 µg pRSV/Rev were co-transfected into 293T cells. After 24 h, the media was removed, cells were washed with phosphate-buffered saline (PBS) and supplemented with fresh media. 48-72 h after transfection, viral supernatants were collected, pooled, filtered through 0.45 mm filters, supplemented with 8 µg/ml polybrene, and used to infect target cells. 24 h after viral transduction, media was removed, cells washed with PBS and supplemented with fresh media specific to the target cell line and selected in appropriate antibiotics. Multiple genes were introduced by sequential infection and drug selection.

Growth curves. Cells were seeded at $2.5x10^4$ cells/well in 6-well dishes. At the appropriate times, cells were washed with PBS, fixed in 10% formalin, rinsed with water, stained with 0.1% crystal violet (Millipore Sigma) for 30 min, rinsed extensively, and dried. Dye was extracted with 10% acetic acid and absorbance measured at 590 nm. All values were normalized to day 0 (24 h after plating). Growth curves were plotted using GraphPad Prism 9.2.0.

Colony forming assays. 4000 cells (A549, A375 and PC3) and 10,000 cells (H1299) or their respective derivatives were plated on 100 mm culture dishes. After 10-14 days in culture, colonies were fixed in 4% formaldehyde in PBS for 10 min, stained with 0.4% crystal violet for 30 min, rinsed thoroughly with water, dried and scanned. The number of colonies were counted using FIJI/ImageJ software v1.53f51 (PMID 22743772).

Senescence-associated β-Galactosidase (SA-βGal) assays

A549 cells or their derivatives were plated at $2.5x10^4$ cells per well in 6-well plates. After 2-3 days, cells were stained using a senescence detection kit (Millipore Sigma QIA117) per the manufacturer's instructions.

Immunoprecipitation (IP). $1x10^6$ HEK293T cells were seeded in 10 cm dishes and transfected with DNA combinations using FuGENE6 (Promega) as described above. 48 h after transfection, cells were washed twice with PBS and processed for cell lysis. For IP of endogenous Tollip and exogenously expressed pyo-KSR1, non-denaturing Lysis Buffer (137 mM NaCl, 20 mM Tris pH 8.0, 10% glycerol,1% Triton X-100) was used for cell lysis. Lysis buffer supplemented with freshly prepared protease inhibitors (Protease Inhibitor Cocktail Set I #539131 and Protease Inhibitor Cocktail Set III #539134, Millipore Sigma-Aldrich) and phosphatase inhibitors (Phosphatase Inhibitor Cocktail Set I #524624 and Phosphatase Inhibitor Cocktail Set II #524625; Millipore Sigma-Aldrich), was added directly on the plated cells and lysed for 15 min on ice. Lysates were centrifuged at 13,000 rpm for 5 min, supernatants collected, and protein estimation was performed using Bradford reagent (Bio-Rad Laboratories, #50000006). 2 mg supernatant was used for immunoprecipitation, with 10% of each supernatant reserved for input samples. For IP of

endogenous TOLLIP, cell supernatants/lysates were precleared using 30 µl of a 50% slurry of Protein G Sepharose (GE Healthcare, #17-0618-01), while for IP of pyo-KSR1, 10µl of Protein G magnetic beads (NEB, S1430S) was used. Precleared supernatant was collected either by centrifugation at 1000 rpm or using a magnetic rack (NEB). Anti-TOLLIP or anti-Glu Glu (pyo) antibody (1:1000) was added to the pre-cleared supernatants and incubated for 1 h at 4°C on a rotating rack. 30µl of 50% slurry of Protein G sepharose or 10µl Protein G magnetic beads were added and incubated at 4°C on a rotating rack for 1 h. Protein G Sepharose beads were pelleted by centrifugation at 1000 rpm for 1 min; magnetic beads were collected using a magnetic rack. Beads were washed 4 times in NET-N Wash Buffer (100mM NaCl, 20 mM Tris pH 8.0, 1 mM EDTA and 0.5% NP40). For IP of Flag-tagged RIOK1, cells were lysed in RIPA buffer (150mM sodium chloride, 50mM Tris pH 8.0, 1% NP-40, 0.1%w/v sodium deoxycholate, 0.10% SDS) 48 h after transfection. Protein G magnetic beads and Anti-Flag antibody (1:1000) were used, and IP was performed as described above except that pre-cleared supernatant was incubated overnight with Anti-Flag primary antibody. 2xSDS sample buffer (Bio-Rad Laboratories) was added to the IP beads and the samples boiled for 7 min at 100°C. Proteins were analyzed by immunoblotting as described below.

Immunoblotting. Cells were harvested after washing twice with cold PBS and lysed with IP lysis buffer or RIPA lysis buffer supplemented with freshly prepared protease and phosphatase inhibitors (see above for details). Cells were lysed on ice for 15 min. Protein samples (30-50 µg) or IP samples were resolved by electrophoresis on 10% or 12% Mini or Midi-TGX Precast Gels (Bio-Rad Laboratories, Cat. nos: 4561034, 4561044, 5671044 and 5671034) and transferred to PVDF membranes (Bio-Rad Laboratories, Cat. no. 1704273). The blots were probed with the

appropriate primary antibodies followed by goat anti-rabbit IgG or goat anti-mouse IgG conjugated to horseradish peroxidase and visualized using enhanced chemiluminescence substrate (SuperSignal™ West Dura Extended Duration Substrate #34076, Thermo Fisher Scientific).

Live cell imaging. $1x10^4$ cells were plated in glass-bottomed chambers (Sarstedt Cat. no. 94.6190.402) or µ-Slides VI0.4 (Ibidi) and cultured for 24 h. Cells were then infected with supernatants of the appropriate lentiviral vectors. After 18-24h, media was replaced, and cells were grown in DMEM+10%FBS for 24h. Next day, media was replaced with DMEM +0.1% FBS and kept overnight. Cells were imaged using a Zeiss LSM-780 confocal microscope equipped with an incubation chamber maintained at 37°C in 5% CO_2.

Immunofluorescence (IF). $1x10^4$ cells were plated in glass-bottomed chambers (Sarstedt, Cat. no. 94.6190.402) or µ-Slides VI0.4 (Ibidi) and cultured for 24 h. Cells were serum starved overnight and, fixed with ice cold 100% methanol for 20 min. The fixed cells were incubated for 1 h in blocking buffer [5% Normal Goat Serum (Cell Signaling) in PBS with 0.3% TritonX100 (Sigma)]. Thereafter, the cells were incubated with the appropriate primary antibodies (1:1000 dilution) overnight at 4°C in blocking buffer. Following 4 washes with IF wash buffer (PBS containing 1% BSA and 0.1% TritonX100), cells were incubated with Alexa 488 and Alexa 594 conjugated secondary antibodies (1:1000) made in IF wash buffer for 1 h at RT. The cells were then washed 4 times and stained with 0.1 µg/mL DAPI (Thermo Fisher Scientific) in PBS for 12 min at room temperature followed by 3 washes with PBS. Fluorescence images were acquired using a Zeiss LSM-780 confocal microscope. For IF of tumor samples, dissected tumor-bearing lungs or pancreata embedded in paraffin blocks (described above); were dissected and 5µm

sections were prepared and slides processed for immunofluorescence. Briefly, slides were deparaffinized using xylene, rehydrated by treating with sequentially decreasing concentrations of ethanol, and antigen retrieval performed using sodium citrate buffer (10mM sodium citrate, 0.05% Tween 20 and 1M HCl). Thereafter, the slides were washed with PBST, fixed in ice-cold methanol for 10 min at -20°C, permeabilized with 1% TritonX100 for 15 min at RT and 1% SDS for 10 min at RT; all steps were interspersed with 3 PBS washes. Slides were blocked using 5% goat serum with 0.3% TritonX-100 in PBS, followed by overnight incubation with rabbit primary antibodies targeting Tollip, KSR1, CK2a or p-ERK at 1:500 dilution in blocking buffer, followed by washing with IF wash buffer (0.1% Triton X-100/1% BSA in PBS) and incubating with Alexa 594 conjugated secondary anti-rabbit antibody (1:500 dilution in IF wash buffer) for 1 h at RT. DAPI staining was performed as described above and the slides were mounted on cover slips using Vecta-shield mounting media (VECTASHIELD® Antifade Mounting Medium, H-1000, VectorLabs). Fluorescence images were acquired using a Zeiss LSM-780 confocal microscope.

Fluorescence-based image analysis. Proximity of punctate fluorescence signals to the cell nucleus was measured in a manually-selected lateral (XY) confocal slice using the image analysis software, FIJI/ImageJ software v1.53f51. Using the reference of the Differential interference contrast (DIC) image and the DAPI stained nucleus, the cell border was drawn manually around the cell cytoplasm and the nuclear border was drawn around the cell nucleus. Then a Fiji macro (available with instructions from the authors upon request) performed the proximity analysis. The macro first required the user to set a threshold intensity to discriminate punctate fluorescence signals from background intensity. Then the macro automatically made 4 calculations: 1. The area of the cytoplasm, 2. The total intensity of the fluorescence signals above the manually set threshold

intensity (The macro did not subtract the background intensity from the fluorescence signals.), 3. The closest distance to the border of the nucleus calculated for each pixel in the cytoplasm (excluding the nucleus), using the Euclidean distance transform, and then integrated these distance values over the cytoplasm, and 4. The product of the fluorescence intensity above background calculated for each pixel in the cytoplasm (from 2.) and the distance value (from 3.), and then integrated these products over the cytoplasm. The manually set threshold intensity was kept constant in an individual experimental set. The 4 values from these 4 calculations were used to calculate the average distance of the fluorescence signals from the edge of the nucleus, which is the value from 4. divided by the value from 2, and to calculate the average distance a uniform signal in the cytoplasm would have from the edge of the nucleus, which is the value from 3. divided by the value from 1. The ratio of the average distance of the fluorescence signals from the edge of the nucleus to the average distance a uniform signal in the cytoplasm would have from the edge of the nucleus was calculated from each cell. If the ratio is statistically significantly above 1 then the fluorescence signals are further away from the nucleus than a uniformly distributed signal. If the ratio is statistically significantly below 1 then the fluorescence signals are closer (proximal) to the nucleus than a uniformly distributed signal.

Proximity ligation assay (PLA). $1x10^4$ A549 cells were grown on glass bottom µ-Slides VI0.4 (Ibidi). PLA was performed using the Duolink *in situ* PLA kit according to the manufacturer's instructions (Millipore Sigma, DUO92002 , DUO92004 and DUO92014). In brief, cells were fixed with pre-chilled MeOH for 15 min at -20ºC and permeabilized with 0.05% Saponin in PBS. After blocking, the cells were incubated overnight at 4°C with the appropriate combinations of antibodies. PLA Plus and Minus probes for mouse and rabbit antibodies (used at 1:5 dilution in

Duolink® Antibody Diluent) were added and incubated for 1 h at 37°C in a pre-heated humidified chamber. The proximity ligation reaction and the polymerase-based DNA amplification reaction were performed for 30 min and 1 h 40 min, respectively, at 37ºC. Samples were counterstained with DAPI for 12 min and images were acquired using a Zeiss LSM-780 confocal microscope. PLA spots were quantified using FIJI/ImageJ software v1.53f51.

RNA FISH. 1×10^4 A549 cells were plated on µ-Slides VI0.4 (Ibidi). 48h after seeding, cells were washed in Cytoskeleton buffer (CB; 10 mmol/L MES pH 6.1, 150 mmol/L NaCl, 5 mmol/L $MgCl_2$, 5 mmol/L EGTA, and 5 mmol/L glucose;) and permeabilized/fixed in ice-cold pre-fixative mix (4% paraformaldehyde, 0.01% glutaraldehyde, 0.05% saponin, in CB) for 20 min at 4°C. Cells were then incubated with ice-cold fixative mix (4% paraformaldehyde, 0.01% glutaraldehyde, in CB) for 100 min at 4°C. Fixed cells were washed with CB twice and quenched by addition of 50 mmol/L NH_4Cl in CB for 5 min at RT. Protease digestion (1:2000 dilution) was performed for 10 min at RT using Protease-QS solution in PBS followed by 2 washes with 1X PBS. For RNA FISH, QuantiGene ViewRNA ISH Cell Assay (Thermo Fisher Scientific) was used according to the manufacturer's protocol. A custom-made probe for human pre-18S rRNA 5'ITS1 (internal transcribed spacer 1) sequence 5′-CCTCGCCCTCCGGGCTCCGTTAATGATC-3′ was used for RNA FISH[47]. Cells were washed four times with PBS-S (0.05% Saponin, in PBS) for 5 min at 20°C, counterstained with DAPI for 10 min at RT, and then washed twice with 1X PBS. Images were acquired using a Zeiss LSM-780 confocal microscope. Image analysis was performed using FIJI/ImageJ software v1.53f51. Briefly, cell border and nuclear border were drawn and marked as region of interest (ROI) and the number of particles (mRNA spots/signal) within the ROI were calculated. The number of cytoplasmic signals was calculated as the number of 5'ITS1 FISH

signals within the cell border subtracted by the number of signals within the nuclear border. The total number of 5'ITS1 FISH signals per cell and the ratio of cytoplasmic to nuclear FISH signals per cell were plotted using GraphPad Prism 9.2.0.

Cell processing for phospho-proteomic analysis. $2x10^6$ NIH3T3 cells were seeded in 150mm plates and cultured for 24 h in DMEM media containing 10% calf serum. The media was replaced by DMEM containing 0.1% calf serum for 24 h, after which the cells were stimulated with 15% calf serum and harvested at 0.5, 2, 4, 6 and 8 h. For harvesting, cells were washed twice with cold PBS, collected by scraping gently using a Cell Lifter (Corning Incorporated, 3008) and centrifuging at 1200 rpm for 3 min. Cells were harvested and used for phospho-proteomic analysis. Three independent replicate experiments were performed. $2x10^6$ $p19^{Arf-/-}$ and $p19^{Arf-/-}$;$Tollip^{-/-}$ MEFs were plated on 100mm plates and transduced with control or $KRAS^{G12V}$ lentiviral vectors. Media was replaced the next day. 24 h later the cells were trypsinized, transferred to a 150mm plate, selected using puromycin (2.5µg/ml) for 2 days and harvested as mentioned above. The experiment was performed using three independent MEF isolates for each genotype. $1x10^6$ A549 were seeded in 100mm plates and infected with lentiviruses expressing control shRNA or three different TOLLIP shRNAs. Media was replaced the next day. After 24 h, cells were trypsinized, transferred to a 150mm plate, and selected using puromycin (2.5µg/ml) for 2 days and harvested as described above. Three replicate experiments were performed for each shRNA construct.

Phospho-proteomic analysis by mass spectrometry. Serum stimulated or unstimulated (0 h) NIH3T3 cells were harvested (see above) and lysed in 500µl urea lysis buffer (8M Urea; 50mM Hepes pH 8.3), sonicated on ice 3 times at 1 min intervals followed by centrifugation at 14,000

rpm for 10 min at 4°C. Supernatants were collected and protein concentrations analyzed using BCA reagent (Bio-Rad). 250 mg protein was taken from each sample and the total volume was adjusted to 150 ul with 50 mM Hepes pH 8.3. The samples were then treated with 10mM DDT for 30 min at room temperature. Samples were alkylated using 20mM 2-Iodoacetamide for 30 min in the dark. 900µl of cold acetone was added to each sample and left overnight at -20°C to precipitate proteins. The samples were centrifuged at 14,000 rpm for 10 min at 4°C and the protein precipitates were collected and resuspended in 50mM Hepes (pH 8.3). Next, the protein samples were treated with 6.5µg trypsin and incubated overnight at 37°C to generate tryptic peptides. The peptide samples were then dried under vacuum and resuspended in 100µl of 50mM Hepes (pH 8.3). Tandem mass tag (TMT) isobaric labeling (ThermoFisher, CA) was performed at 1:4 ratio by weight of sample for 1 h, and the reaction was quenched with 5% hydroxylamine. Different mass tags were used for peptides obtained from the NIH3T3 cells harvested at different time points of serum stimulation, while technical replicates received the same mass tags. Samples were mixed, concentrated, dried under vacuum, and resuspended in 0.1% trifluoroacetic acid. To remove any uncoupled TMT, peptide samples were passed through empty C18 columns (ThermoFisher, CA). Eluted TMT labeled peptides were enriched for phosphopeptides by TiO_2 affinity purification (High Select TiO_2 kit; Thermo-Scientific, #A32993). The enriched phosphopeptides bound to TiO_2 beads were eluted by high pH solvent and dried under vacuum. The flow through peptides and the phosphopeptides obtained from the various wash steps were collected separately, dried under vacuum, and resuspended in 0.1% TFA and further enriched for phosphopeptides using Fe-Oxide affinity purification (High Select Fe-NTA; Thermo-Scientific, #A32992). The phosphopeptides on the Fe-Oxide beads were then eluted by high pH solvents and combined with the TiO_2 eluate collected earlier to obtain the maximum yield of phosphopeptides. The enriched phosphopeptides

were fractionated by high pH (8.5) reverse phase (RP) on Waters Acquity UPLC system coupled to fluorescence detector (Waters, Milford, MA). The fractions were consolidated into 12 pools based on the chromatographic intensity. The flow-through and the wash solutions of the Fe-oxide steps were collected, dried under vacuum, fractionated by high pH (8.5) RP chromatography, and consolidated into 24 pools based on the chromatographic intensity. The fraction pools were lyophilized and stored at -80ºC until analyzed by mass spectrometry.

For MEFs, three biological replicates of $p19^{Arf-/-}$ (denoted WT), $p19^{Arf-/-}$ expressing $KRAS^{G12V}$ (denoted KRAS:WT), $p19^{Arf-/-}$;$Tollip^{-/-}$ (denoted Tollip), and $p19^{Arf-/-}$;$Tollip^{-/-}$ expressing $KRAS^{G12V}$ (denoted KRAS:Tollip) were used. The protein lysates were processed as mentioned above. Different mass tags were used for the different cell types (WT, KRAS:WT, Tollip, and KRAS:Tollip), while biological replicates received the same mass tags. Phospho-peptides were enriched using TiO_2 affinity purification and Fe-Oxide affinity-purification and fractionated using high pH (8.5) RP. The fraction pools were then lyophilized and stored at -80ºC.

For A549 cells, each TMT run contained four channels: an A549 control run and three A549 samples treated with three different TOLLIP shRNAs. Each of these four channels were run in three independent TMT runs, resulting in 12 different intensities of phospho-peptides. TMT labeling and phospho-peptide enrichment were performed as mentioned above. Different mass tags were used for the different cell types, while technical replicates received the same mass tags. Phospho-peptides were enriched using TiO_2 affinity purification and Fe-Oxide affinity-purification, fractionated and the resulting fraction pools were lyophilized and stored at -80ºC.

Mass spectrometry data acquisition and analysis. The data acquisition of TMT labeled peptides from NIH 3T3 cells was performed using Fusion Orbitrap (Thermo Scientific) and the data for A549 and MEF cells were acquired using a Q-Exactive HF mass spectrometer (Thermo

Scientific). The dried samples were reconstituted in 0.1% TFA and separated using a second dimension low pH gradient using a nanoflow liquid chromatography (Thermo Easy nLC 1000, Thermo Scientific) coupled to a mass spectrometer at 300 nl/min. The MS/MS analysis of the peptides along with the quantitative analysis of the TMT tags were performed at high resolution of 50,000 (Fusion)/45,000 (HF) in the orbitrap analyzer. Acquired MS/MS spectra were searched against mouse (for NIH 3T3 and MEFs) or human (for A549) Uniprot protein databases along with a contaminant protein database, using a SEQUEST and percolator validator algorithms in the Proteome Discoverer 2.2 software (Thermo Scientific, CA). The precursor ion tolerance was set at 10 ppm and the fragment ions tolerance was set at 0.02 Da along with methionine oxidation included as dynamic modification and TMT6 plex (229.163Da) set as a static modification of lysine and the N-termini of the peptide. For phospho-enriched peptides, phosphorylation of serine, threonine and tyrosine was set as a dynamic modification. Trypsin was specified as the proteolytic enzyme, with up to 2 missed cleavage sites allowed. A reverse decoy database search strategy was used to control for the false discovery rate and peptide identifications were validated using the percolator algorithm. Phospho-peptides and flow-through peptides from three independent experiments were analyzed. The affinity purified peptides were used to determine the abundance of phospho-peptides (denoted p-peptides) while the flow-through peptides were used to measure the abundance of the proteins.

Bioinformatic analysis of LC-MS data. All of the analysis using the MTM LC/MS/MS p-peptide and protein intensities were performed using either R (Version 4.1.2) or in-house programs. The first step in analyzing the LC-MS data for the serum-stimulated NIH3T3 cells was to process the TiO_2-enriched peptides. Only phosphorylated peptides were considered for analysis. This was

followed by examining each phospho-peptide and removing from consideration any that could belong to more than one protein. Phospho-peptides and all proteins identified in the flow-through sample were required to have at least two valid intensities across the three replicates for each of the six time points and the pooled sample. Each technical replicate at each time point for the phospho-peptides and proteins was then subjected to a MAS5 normalization, treating each replicate/time point independently. Due to the variability in the distribution of missing intensities between replicates and time points, some may have missing values for more than 5% of the phosphopeptides or proteins and were included as zeroes in the MAS5 normalization. Therefore, each set of replicate/time point values across the phospho-peptides or proteins was rescaled to have a constant maximum value. Finally, the internal reference scaling (IRS) method [67] was used to scale each replicate and time point relative to the pooled sample for both the phospho-peptide and protein intensities. For each replicate at each time point, the phospho-peptide/protein ratios were then calculated. In this analysis, valid ratios are required for all three replicates at each time point. The phospho-proteomic data was then filtered for p-peptides that increased by ≥1.5-fold at 4 and/or 6 h relative to unstimulated (0 h) cells and also increased ≥1.2-fold versus 0.5 and 2 h. Phospho-sites that passed these tests in at least 2 of 3 replicates were analyzed further. The amino acid sequence around the phosphorylation site of phospho-peptides was examined to determine if it represented a CK2 phosphorylation motif, [S|T]xx[D|E][43]. DAVID analysis[68] was performed to determine functional annotation of the potential CK2 phospho-peptides. Functional classifications based on Molecular Function (GOTERM_MF_DIRECT) and Biological Processes (GOTERM_BP_DIRECT) were obtained and plotted. Ingenuity Pathway Analysis (IPA) software[69] was used to perform "Phosphorylation Analysis". In this analysis, the total phospho-peptide dataset enriched at 4 and/or 6 h (see above) was used to generate phosphorylation/signaling

networks. Briefly, proteins corresponding to the phospho-peptides from our analysis were used as identifiers and uploaded into the application. Networks generated by the IPA analysis are indicative of potential signaling cascades.

For MEF data, combining the results from the three independent experiments produced two datasets containing 12 channels: one dataset for the p-peptides and the other for the proteins. The 12 channels represent the three technical replicates for WT, KRAS:WT, Tollip, and KRAS:Tollip. The first step in the analysis was to remove any p-peptide or protein from the datasets that did not contain a measured intensity in all 12 channels. Each dataset was then normalized to a constant total intensity for each of the 12 channels. The mean total intensity across the 12 channels was used as the normalization factor. The next step was to calculate the p-peptide/protein ratio in each of the 12 channels. For each p-peptide, the Master Protein identifier was used to search for the same identifier in the protein dataset, and if found, the 12 p-peptide/protein ratios were determined. From these the KRAS:WT/WT and KRAS:Tollip/Tollip ratios were calculated for each replicate, and then compared to produce a (KRAS:WT/WT)/(KRAS:Tollip/Tollip) fold-change ratio for each replicate. The arithmetic mean across three replicates for KRAS:WT/WT, KRAS:Tollip/Tollip and (KRAS:WT/WT)/(KRAS:Tollip/Tollip) was then determined for each p-peptide that had 12 observed p-peptide/protein ratios. Each of these three sets of mean ratios were log-transformed to produce a normal distribution and the 90% confidence interval was determined. Those p-peptides whose (KRAS:WT/WT)/(KRAS:Tollip/Tollip) ratio was above the upper bound of the 90% confidence interval were identified. From the overall set of p-peptide with 12 peptide/protein ratios, the fraction of p-peptides with phosphorylation at a CK2 motif was determined using the reference CK2 phosphorylation motif, [S|T]xx[D|E]. For each set of selected p-peptides, e.g., those

p-peptides whose (KRAS:WT/WT)/(KRAS:Tollip/Tollip) log-ratio was greater than the upper 90% confidence interval, the number containing phosphorylations at CK2 motifs was compared to the number expected by chance, and a Binomial test was used to determine if the difference from expected was significant. Functional annotation of CK2 p-peptides was performed using DAVID and IPA analysis of the total phospho-peptide dataset was used to generate potential signaling networks.

For phospho-proteomic analysis of A549 cells, the first step was to remove any phospho-peptide that was not observed in all 12 channels (three replicates of control and *TOLLIP* knockdown A549 cells). This was done for both the phospho-peptides and the proteins. The second step was to scale the observed intensities so that the total intensity for each of the 12 phospho-peptide channels was set to an arbitrary constant ($1x10^{11}$ in this analysis). A similar procedure was applied to the protein intensities where the total intensity in each channel was set to $1x10^{12}$. This was done using R (version 4.1.2). The third step was to calculate the peptide/protein ratios in each of the 12 channels. An in-house program used the protein Accession number from the peptide file and matched it to the correct protein in the protein file. The arithmetic mean of the peptide/protein ratios across the three technical replicates was then determined for control and TOLLIP knockdown cells using R. These arithmetic means were then used to identify the phospho-peptides that were reduced by at least a factor of 1.2 in each of the Tollip knockdowns relative to the control A549 set. Potential phospho-peptides were scanned using the reference CK2 phosphorylation motif, [S|T]xx[D|E], as described above, and functional annotation was performed using DAVID. IPA analysis of the total phospho-peptide dataset was used to generate potential signaling networks.

Statistical analysis. Statistical analysis was performed using GraphPad Prism. Statistical significance for quantitation of immunoprecipitation experiments, colony formation assays and SA-βGal assay was calculated using Student's t test. P values less than 0.05 were considered significant. The log-rank (Mantel-Cox) test was used for Kaplan–Meier survival analyses. Two-way ANOVA was used to analyze growth curves.

References

1. Prior, I.A., Hood, F.E. & Hartley, J.L. The Frequency of Ras Mutations in Cancer. *Cancer Research* **80**, 2969-2974 (2020).
2. Schneider, G., Schmidt-Supprian, M., Rad, R. & Saur, D. Tissue-specific tumorigenesis: context matters. *Nat Rev Cancer* **17**, 239-253 (2017).
3. Baines, A.T., Xu, D. & Der, C.J. Inhibition of Ras for cancer treatment: the search continues. *Future Med Chem* **3**, 1787-1808 (2011).
4. Konieczkowski, D.J., Johannessen, C.M. & Garraway, L.A. A Convergence-Based Framework for Cancer Drug Resistance. *Cancer Cell* **33**, 801-815 (2018).
5. Tape, C.J. *et al.* Oncogenic KRAS Regulates Tumor Cell Signaling via Stromal Reciprocation. *Cell* **165**, 1818 (2016).
6. Gober, M.K. *et al.* Deregulation of a Network of mRNA and miRNA Genes Reveals That CK2 and MEK Inhibitors May Synergize to Induce Apoptosis KRAS-Active NSCLC. *Cancer Inform* **18**, 1176935119843507 (2019).
7. Wang, H. *et al.* An integrative pharmacogenomics analysis identifies therapeutic targets in KRAS-mutant lung cancer. *EBioMedicine* **49**, 106-117 (2019).
8. Papke, B. & Der, C.J. Drugging RAS: Know the enemy. *Science* **355**, 1158-1163 (2017).
9. Moore, A.R., Rosenberg, S.C., McCormick, F. & Malek, S. RAS-targeted therapies: is the undruggable drugged? *Nat Rev Drug Discov* **19**, 533-552 (2020).
10. Network, T.C.G.A.R. Comprehensive molecular profiling of lung adenocarcinoma. *Nature* **511**, 543-550 (2014).

11. Yip-Schneider, M.T., Lin, A., Barnard, D., Sweeney, C.J. & Marshall, M.S. Lack of elevated MAP kinase (Erk) activity in pancreatic carcinomas despite oncogenic K-ras expression. *Int J Oncol* **15**, 271-279 (1999).
12. Omerovic, J., Hammond, D.E., Clague, M.J. & Prior, I.A. Ras isoform abundance and signalling in human cancer cell lines. *Oncogene* **27**, 2754-2762 (2008).
13. Yeh, J.J. *et al.* KRAS/BRAF mutation status and ERK1/2 activation as biomarkers for MEK1/2 inhibitor therapy in colorectal cancer. *Mol Cancer Ther* **8**, 834-843 (2009).
14. Lim, K.H. *et al.* Activation of RalA is critical for Ras-induced tumorigenesis of human cells. *Cancer Cell* **7**, 533-545 (2005).
15. Mizumoto, Y. *et al.* Activation of ERK1/2 occurs independently of KRAS or BRAF status in endometrial cancer and is associated with favorable prognosis. *Cancer Sci* **98**, 652-658 (2007).
16. Gelabert-Baldrich, M. *et al.* Dynamics of KRas on endosomes: involvement of acidic phospholipids in its association. *FASEB J.* **28**, 3023-3037 (2014).
17. Schmick, M. *et al.* KRas localizes to the plasma membrane by spatial cycles of solubilization, trapping and vesicular transport. *Cell* **157**, 459-471 (2014).
18. Basu, S.K., Basu, S. & Johnson, P.F. Localized RAS signaling drives cancer. *Oncoscience* **6**, 298-300 (2019).
19. Cheng, C.M. *et al.* Compartmentalized Ras proteins transform NIH 3T3 cells with different efficiencies. *Mol. Cell. Biol.* **31**, 983-997 (2011).
20. Onken, B., Wiener, H., Philips, M.R. & Chang, E.C. Compartmentalized signaling of Ras in fission yeast. *Proc. Natl. Acad. Sci. USA* **103**, 9045-9050 (2006).
21. Lu, A. *et al.* A clathrin-dependent pathway leads to KRas signaling on late endosomes en route to lysosomes. *J. Cell Biol.* **184**, 863-879 (2009).
22. Teis, D., Wunderlich, W. & Huber, L.A. Localization of the MP1-MAPK scaffold complex to endosomes is mediated by p14 and required for signal transduction. *Dev Cell* **3**, 803-814 (2002).
23. Basu, S.K. *et al.* Oncogenic RAS-Induced Perinuclear Signaling Complexes Requiring KSR1 Regulate Signal Transmission to Downstream Targets. *Cancer Research* **78**, 891-908 (2018).
24. Mellman, I. & Yarden, Y. Endocytosis and cancer. *Cold Spring Harb Perspect Biol* **5**, a016949 (2013).

25. Sigismund, S. *et al.* Endocytosis and signaling: cell logistics shape the eukaryotic cell plan. *Physiol Rev* **92**, 273-366 (2012).
26. Jongsma, M.L. *et al.* An ER-Associated Pathway Defines Endosomal Architecture for Controlled Cargo Transport. *Cell* **166**, 152-166 (2016).
27. Stewart, S. *et al.* Kinase suppressor of Ras forms a multiprotein signaling complex and modulates MEK localization. *Mol. Cell. Biol.* **19**, 5523-5534 (1999).
28. Roy, F., Laberge, G., Douziech, M., Ferland-McCollough, D. & Therrien, M. KSR is a scaffold required for activation of the ERK/MAPK module. *Genes Dev.* **16**, 427-438 (2002).
29. Ritt, D.A. *et al.* CK2 Is a component of the KSR1 scaffold complex that contributes to Raf kinase activation. *Curr Biol* **17**, 179-184 (2007).
30. Shtutman, M. *et al.* Function-based gene identification using enzymatically generated normalized shRNA library and massive parallel sequencing. *Proc. Natl. Acad. Sci. USA* **107**, 7377-7382 (2010).
31. Wolf, J. *et al.* A mammosphere formation RNAi screen reveals that ATG4A promotes a breast cancer stem-like phenotype. *Breast Cancer Res* **15**, R109 (2013).
32. Vizeacoumar, F.J. *et al.* A negative genetic interaction map in isogenic cancer cell lines reveals cancer cell vulnerabilities. *Mol Syst Biol* **9**, 696 (2013).
33. Frodyma, D., Neilsen, B., Costanzo-Garvey, D., Fisher, K. & Lewis, R. Coordinating ERK signaling via the molecular scaffold Kinase Suppressor of Ras. *F1000Res* **6**, 1621 (2017).
34. Michaud, N.R. *et al.* KSR stimulates Raf-1 activity in a kinase-independent manner. *Proc Natl Acad Sci U S A* **94**, 12792-12796 (1997).
35. Jacobs, D., Glossip, D., Xing, H., Muslin, A.J. & Kornfeld, K. Multiple docking sites on substrate proteins form a modular system that mediates recognition by ERK MAP kinase. *Genes Dev.* **13**, 163-175 (1999).
36. Cacace, A.M. *et al.* Identification of constitutive and ras-inducible phosphorylation sites of KSR: implications for 14-3-3 binding, mitogen-activated protein kinase binding, and KSR overexpression. *Mol. Cell. Biol.* **19**, 229-240 (1999).
37. McKay, M.M., Ritt, D.A. & Morrison, D.K. Signaling dynamics of the KSR1 scaffold complex. *Proc. Natl. Acad. Sci. USA* **106**, 11022-11027 (2009).
38. Ciarrocchi, A. *et al.* Tollip is a mediator of protein sumoylation. *PLoS One* **4**, e4404 (2009).

39. Burns, K. *et al.* Tollip, a new component of the IL-1RI pathway, links IRAK to the IL-1 receptor. *Nat Cell Biol* **2**, 346-351 (2000).
40. Shih, S.C. *et al.* A ubiquitin-binding motif required for intramolecular monoubiquitylation, the CUE domain. *EMBO J.* **22**, 1273-1281 (2003).
41. Yamakami, M., Yoshimori, T. & Yokosawa, H. Tom1, a VHS domain-containing protein, interacts with tollip, ubiquitin, and clathrin. *J. Biol. Chem.* **278**, 52865-52872 (2003).
42. Jumper, J. *et al.* Highly accurate protein structure prediction with AlphaFold. *Nature* **596**, 583-589 (2021).
43. Pinna, L.A. Casein kinase 2: an 'eminence grise' in cellular regulation? *Biochim Biophys Acta* **1054**, 267-284 (1990).
44. Meggio, F. & Pinna, L.A. One-thousand-and-one substrates of protein kinase CK2? *FASEB J.* **17**, 349-368 (2003).
45. Preti, M. *et al.* Gradual processing of the ITS1 from the nucleolus to the cytoplasm during synthesis of the human 18S rRNA. *Nucleic Acids Res.* **41**, 4709-4723 (2013).
46. Widmann, B. *et al.* The kinase activity of human Rio1 is required for final steps of cytoplasmic maturation of 40S subunits. *Mol. Biol. Cell* **23**, 22-35 (2012).
47. Turowski, T.W. *et al.* Rio1 mediates ATP-dependent final maturation of 40S ribosomal subunits. *Nucleic Acids Res.* **42**, 12189-12199 (2014).
48. Luo, J. *et al.* A genome-wide RNAi screen identifies multiple synthetic lethal interactions with the Ras oncogene. *Cell* **137**, 835-848 (2009).
49. Weinberg, F. *et al.* The Atypical Kinase RIOK1 Promotes Tumor Growth and Invasive Behavior. *EBioMedicine* **20**, 79-97 (2017).
50. Hong, X. *et al.* Targeting posttranslational modifications of RIOK1 inhibits the progression of colorectal and gastric cancers. *eLife* **7** (2018).
51. Kubinski, K. & Maslyk, M. The Link between Protein Kinase CK2 and Atypical Kinase Rio1. *Pharmaceuticals* **10** (2017).
52. Murphy, J.E., Padilla, B.E., Hasdemir, B., Cottrell, G.S. & Bunnett, N.W. Endosomes: a legitimate platform for the signaling train. *Proc. Natl. Acad. Sci. USA* **106**, 17615-17622 (2009).
53. Pokatayev, V. *et al.* Homeostatic regulation of STING protein at the resting state by stabilizer TOLLIP. *Nat Immunol* **21**, 158-167 (2020).

54. Toruń, A. *et al.* Endocytic Adaptor Protein Tollip Inhibits Canonical Wnt Signaling. *PLoS One* **10**, e0130818 (2015).
55. Zhu, L. *et al.* Tollip, an intracellular trafficking protein, is a novel modulator of the transforming growth factor-β signaling pathway. *J. Biol. Chem.* **287**, 39653-39663 (2012).
56. Li, X., Goobie, G.C. & Zhang, Y. Toll-interacting protein impacts on inflammation, autophagy, and vacuole trafficking in human disease. *Journal of molecular medicine* **99**, 21-31 (2021).
57. Didierlaurent, A. *et al.* Tollip regulates proinflammatory responses to interleukin-1 and lipopolysaccharide. *Mol. Cell. Biol.* **26**, 735-742 (2006).
58. Munroe, D. & Jacobson, A. mRNA poly(A) tail, a 3' enhancer of translational initiation. *Mol. Cell. Biol.* **10**, 3441-3455 (1990).
59. Wells, S.E., Hillner, P.E., Vale, R.D. & Sachs, A.B. Circularization of mRNA by eukaryotic translation initiation factors. *Mol Cell* **2**, 135-140 (1998).
60. Feldser, D.M. *et al.* Stage-specific sensitivity to p53 restoration during lung cancer progression. *Nature* **468**, 572-575 (2010).
61. Johnson, L. *et al.* Somatic activation of the K-ras oncogene causes early onset lung cancer in mice. *Nature* **410**, 1111-1116 (2001).
62. Tuveson, D.A. *et al.* Endogenous oncogenic K-ras(G12D) stimulates proliferation and widespread neoplastic and developmental defects. *Cancer Cell* **5**, 375-387 (2004).
63. Hingorani, S.R. *et al.* Trp53R172H and KrasG12D cooperate to promote chromosomal instability and widely metastatic pancreatic ductal adenocarcinoma in mice. *Cancer Cell* **7**, 469-483 (2005).
64. Therrien, M., Michaud, N.R., Rubin, G.M. & Morrison, D.K. KSR modulates signal propagation within the MAPK cascade. *Genes Dev.* **10**, 2684-2695 (1996).
65. Campeau, E. *et al.* A versatile viral system for expression and depletion of proteins in mammalian cells. *PLoS One* **4**, e6529 (2009).
66. Boothe, T. *et al.* Inter-domain tagging implicates caveolin-1 in insulin receptor trafficking and Erk signaling bias in pancreatic beta-cells. *Mol Metab* **5**, 366-378 (2016).
67. Plubell, D.L. *et al.* Extended Multiplexing of Tandem Mass Tags (TMT) Labeling Reveals Age and High Fat Diet Specific Proteome Changes in Mouse Epididymal Adipose Tissue. *Mol Cell Proteomics* **16**, 873-890 (2017).

68. Sherman, B.T. *et al.* DAVID: a web server for functional enrichment analysis and functional annotation of gene lists (2021 update). *Nucleic Acids Res.* (2022).
69. Kramer, A., Green, J., Pollard, J., Jr. & Tugendreich, S. Causal analysis approaches in Ingenuity Pathway Analysis. *Bioinformatics* **30**, 523-530 (2014).

Figure legends

Fig. 1 | TOLLIP interacts with KSR1 and co-localizes with KSR1 and CK2α on RAB11A+ perinuclear endosomes in tumor cells. a, Co-immunoprecipitation assay showing association of Pyo-KSR1 with endogenous TOLLIP in 293T cells. Quantitation of three experiments is shown on the right. **b**, Live cell imaging shows perinuclear localization of GFP-tagged TOLLIP in A549 lung ADC cells and pan-cytoplasmic distribution in a non-transformed bronchial epithelial cell line, HBEC. Relative nuclear proximity index (RNPI) measures perinuclear clustering of fluorescent signals in each cell (see Methods). Values are averages for A549 cells (n=12) and HBEC cells (n=12). **c**, IF staining of A549 cells demonstrates co-localization of TOLLIP with KSR1, CK2α, and RAB11A but not p-ERK. **d**, TOLLIP-EGFP shows partial co-localization with KSR1-mCherry and nearly complete overlap with CK2α-mCherry and RAB11A-tagRFP in A549 cells. **e**, Proximity ligation assays (PLA) were used to confirm the juxtaposition of TOLLIP with KSR1, CK2α, and KSR1 but not p-ERK in A549 cells. Bottom panel: PLA signal quantification, expressed as positive signals/cell. **f**, Fluorescently labeled KSR1, CK2α, TOLLIP and RAB11A are present on vesicles embedded within the Sec61β-GFP positive ER network in A549 cells. Scale bars, 10 μm. Statistical significance for quantitation of immunoprecipitation and RNPI was calculated using Student's t test; * $p \leq 0.05$.

Fig. 2 | TOLLIP silencing disrupts perinuclear localization of CK2α and KSR1 and decreases proliferation/survival of tumor cells but not normal cells. a, TOLLIP depletion in A549 cells causes pan-cytoplasmic dispersal of KSR1, CK2α and RAB11A. **b**, TOLLIP ablation impairs proliferation of A549 and PANC1 tumor cells. **c**, TOLLIP-depleted A549 cells display increased

senescence (SA-βGal positivity) and apoptosis (cleaved CASPASE-3). **d**, TOLLIP silencing does not affect the growth rate of HBEC cells. **e**,**f**, RAB11A knockdown results in more uniform cytoplasmic distributions of TOLLIP, KSR1 and CK2α.

Two-way ANOVA was used to analyze growth curves. Student's t-test was performed for SA-βGal assay; * $p \leq 0.05$.

Fig. 3 | TOLLIP and KSR1 interact through conserved domains in each protein. a, Mapping the KSR1-interacting region of Tollip. HA-tagged full-length and mutant rat Tollip proteins were co-expressed with Pyo-KSR1 in HEK293T cells. Input lysates and Pyo IP samples were analyzed by immunoblotting for HA (Extended Data Fig. 3b). Binding intensity (IP/input) was determined by averaging three experiments and the data were normalized to WT Tollip. TBD, TOM1 binding domain; C2, lipid binding domain; CUE, ubiquitin binding domain. **b**, The KSR1 binding region of Tollip includes an 18 aa core sequence (185-202) that is conserved among vertebrate homologs. The alignment shows six vertebrate and three invertebrate Tollip sequences spanning the core KSR1 binding motif (highlighted). **c,** A model of human TOLLIP predicted by AlphaFold2[42] shows the KSR1 binding sequence forming a β-hairpin fold. Arrows point to the boundaries of the conserved 18 aa core. *C. elegans* Tollip (right), lacking the conserved KSR1 binding sequence, is not predicted to form a corresponding β-hairpin.

Student's t-test was performed for IP quantification; * $p \leq 0.05$.

Fig. 4 | *Tollip* is a dependency gene selective for *KRAS*-transformed cells. a, Oncogenic *HRAS* and *KRAS* induce perinuclear translocation of CK2α and KSR1 in NIH3T3 cells but Tollip-dependence is restricted to *KRAS*-transformed cells. Control (left) or Tollip knockdown (right)

NIH3T3 cells were infected with lentiviruses carrying *HRAS*^{G12V}, *KRAS*^{G12V} or no insert (Ctrl) and immunostained for CK2α and KSR1. **b**,**c**, Proliferation of *RAS*-transformed or control NIH3T3 cells was analyzed without and with Tollip depletion. **b**, *KRAS*^{G12V} cells; **c**, *HRAS*^{G12V} cells. The same growth curves for non-transformed cells are shown in the two figures as the experiment was performed with common control cells. **d**, TOLLIP silencing does not significantly affect proliferation of T24 cells (human urinary bladder carcinoma; *HRAS*^{G12V}). **e**, Perinuclear partitioning of KSR1 and CK2α in T24 cells is unaffected by TOLLIP depletion.

The means ± s.d. are shown; n=3 independent experiments. Statistical analysis was performed using the using Two-way ANOVA test; * $p \leq 0.05$.

Fig. 5 | Tollip is required for progression to adenocarcinoma in a *Kras*^{G12D}-driven model of lung tumorigenesis. **a**, Kaplan-Meier curves of *Tollip*$^{+/+}$*;LSL-Kras*^{G12D} and *Tollip*$^{-/-}$*;LSL-Kras*^{G12D} mice following intratracheal instillation of Ad.Cre virus in 10-week-old mice to initiate lung tumorigenesis. **b**, Representative examples of H&E images for lung hyperplasia, adenoma and adenocarcinoma from *WT* animals. **c**, Hyperplasia and total lung tumor burdens in the two strains at clinical sacrifice, as measured by HALO image analysis (% of lung area). **d**, Incidence of lung adenocarcinoma is reduced in *Tollip*$^{-/-}$ mice. The graph shows most severe tumor grade observed from histopathological examination (% animals for each genotype). **e**, Lung lesions observed in Athymic *nu/nu* mice five weeks after tail vein injection of $1x10^6$ A549 cells. Cells were infected with a control lentivirus (shCtrl) or two different TOLLIP shRNA-expressing vectors prior to injection. Cells lacking TOLLIP produced a maximum of two lung nodules per animal. TOLLIP knockdown efficiency was verified by immunoblot analysis of each cell population (left).

The log-rank (Mantel-Cox) test was used for Kaplan–Meier survival analyses. Statistical significance for quantitation of hyperplasia and tumor burden was calculated using Student's t test. Fisher's exact test was used to compare lung adenocarcinoma incidence in *WT* and *Tollip*$^{-/-}$ mice. * $p \leq 0.05$.

Fig. 6 | Characterization of phosphoproteomes coinciding with PSC formation in GF-stimulated and *KRAS*-transformed cells. a, Phosphoproteomic analysis pipeline for serum-stimulated NIH3T3 cells. KSR1 and CK2α form PSCs at 4 and 6 h, and p-ERK becomes perinuclear at 6 h[23]. Tollip also undergoes perinuclear translocation at 4 and 6 h (not shown). **b**, Frequency of CK2 sites in p-peptides that increase at 4 and/or 6 h. **c**, List of common p-peptides up-regulated at both 4 and 6 h that correspond to predicted or known CK2 sites. **d-f**, Gene ontology (DAVID bioinformatics, molecular function) of proteins corresponding to p-peptides (CK2 sites) increased at 4 and/or 6 h. The most enriched GO terms are shown, plotted as -$\log_{10}$(Pvalue). **g**, List of proteins corresponding to TOLLIP-dependent p-peptides (CK2 sites) in control vs. TOLLIP-depleted A549 cells (90% confidence interval). **h**, Ranked GO terms (molecular function) for proteins shown in (**g**). **i**, List of proteins corresponding to *KRAS*^{G12V}-induced p-peptides (CK2 sites) preferentially increased in *WT* vs. *Tollip*$^{-/-}$ MEFs (90% CI). MEFs also lacked *p19*^{Arf} to allow transformation by *KRAS*^{G12V}. P-peptides are ranked by *KRAS*-induced fold change ratio [FC(*WT*):FC(*Tollip*$^{-/-}$)]. FC values (*KRAS*:Ctrl) for the corresponding p-peptides in each MEF genotype are shown on the left. **j**, Ranked GO terms (DAVID, molecular function) for proteins shown in (**i**). **k**, p-peptides (CK2 sites) common to at least 2 of 3 data sets (NIH3T3, MEFs and A549 cells). **l**, Proteins common to at least 2 of 3 data sets. Bottom panel: ranked GO terms (molecular function) for this set of proteins.

Fig. 7 | TOLLIP-dependent phosphorylation of RIOK1 on the CK2 site, Ser21/Ser22, stimulates its pro-oncogenic function in tumor cells. a, RIOK1 Ser21/Ser22 and flanking sequences are conserved in mammalian proteins and absent in other species homologs, including other vertebrates. **b**, RIOK1 Ser21/Ser22 undergo *KRAS*^{G12V}-induced, TOLLIP-dependent phosphorylation. Flagged-tagged RIOK1 *WT* and S21A/S22A mutant constructs were expressed in control and TOLLIP-depleted HEK293T cells, ± *KRAS*^{G12V}. Lysates were immunoprecipitated with Flag antibody and samples were analyzed by immunoblotting using pan-CK2 substrate Ab or Flag Ab. p-RIOK1 levels normalized to total RIOK1 in FLAG IP samples is shown on the right. **c,** RIOK1 is essential for clonogenic growth of A549 cells. RIOK1 was depleted using two different shRNA constructs and cells were analyzed for colony formation. **d**, Ser21/Ser22 are required for RIOK1 function in A549 cells. RIOK1 was depleted in A549 cells using an shRNA targeting the *RIOK1* 3'UTR, and *WT* and mutant shRNA-resistant constructs lacking the 3'UTR were expressed to assess their ability to rescue clonogenic growth. The immunoblot shows RIOK1 depletion and levels of over-expressed FLAG-RIOK1 proteins. **e**, TOLLIP and RIOK1 are required for efficient 18S rRNA processing. A549 cells were depleted for RIOK1 or TOLLIP and analyzed by RNA FISH using a 5'ITS probe to detect the unprocessed 18S precursor (upper panel). Number of FISH signals and the cytoplasmic/nuclear ratio per cell were quantified (lower panel). Student's t-test was used to analyze the 5'ITS1 RNA FISH data; * $p \leq 0.05$.

Figure 1

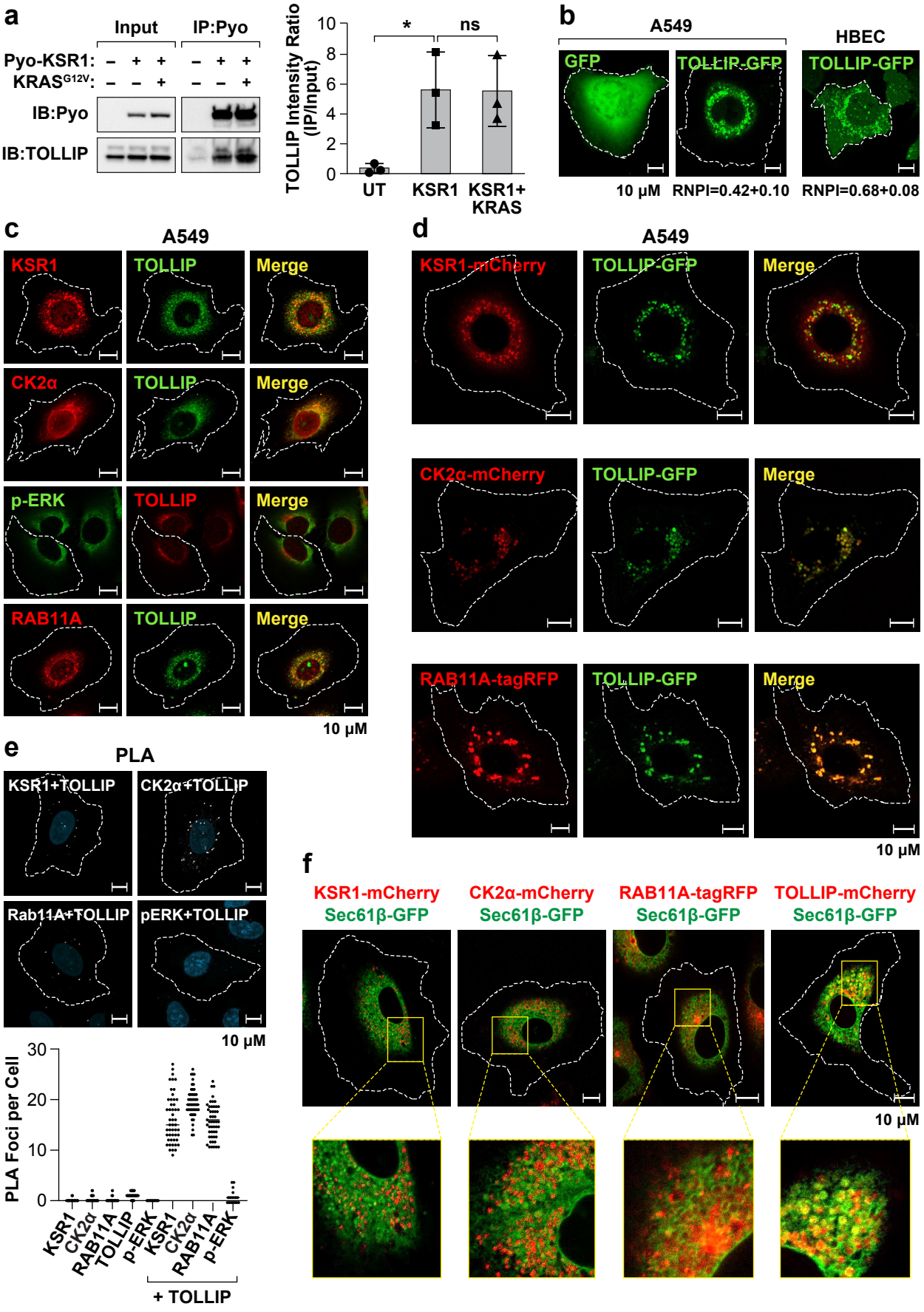

Figure 2

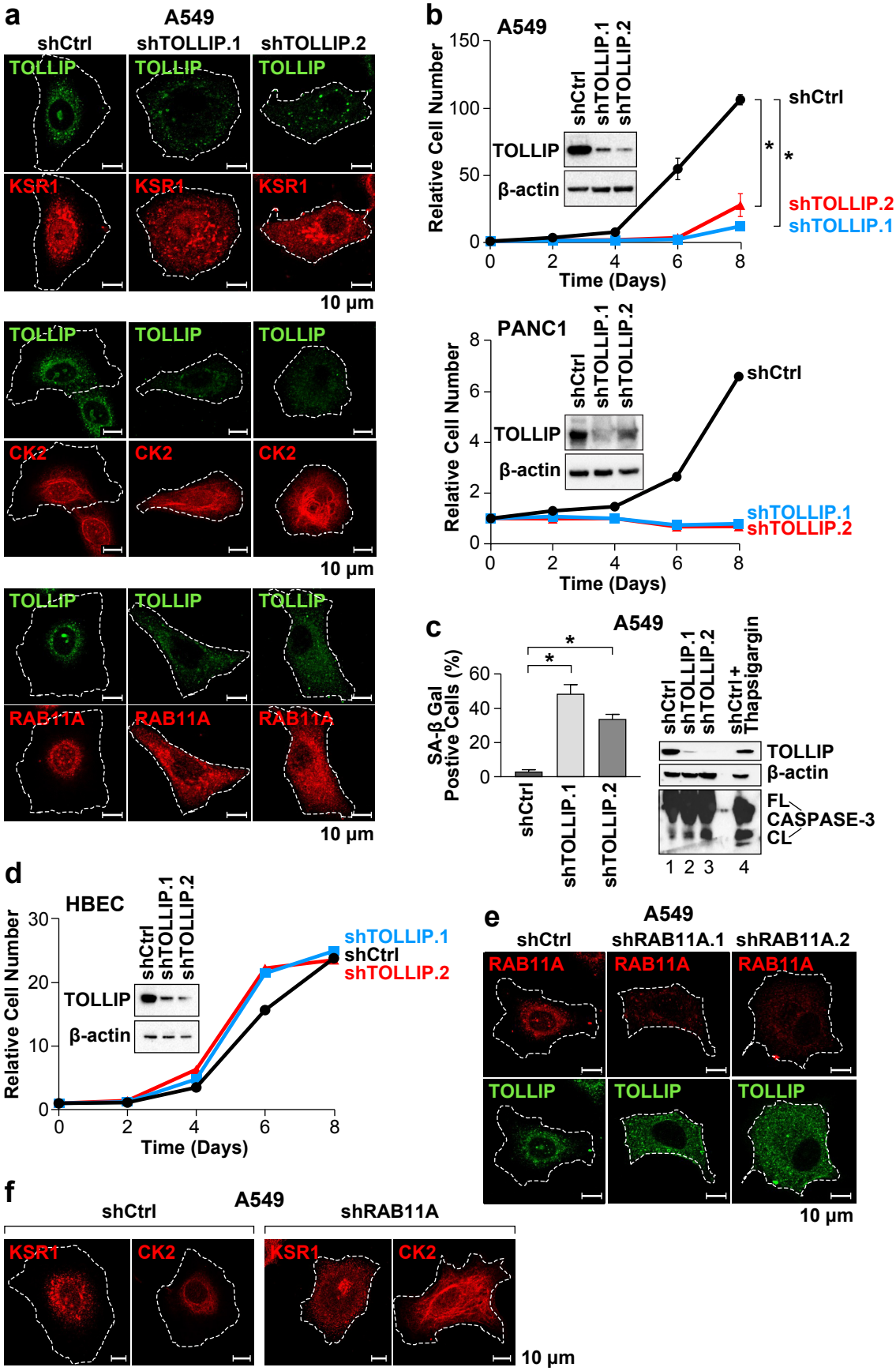

Figure 3

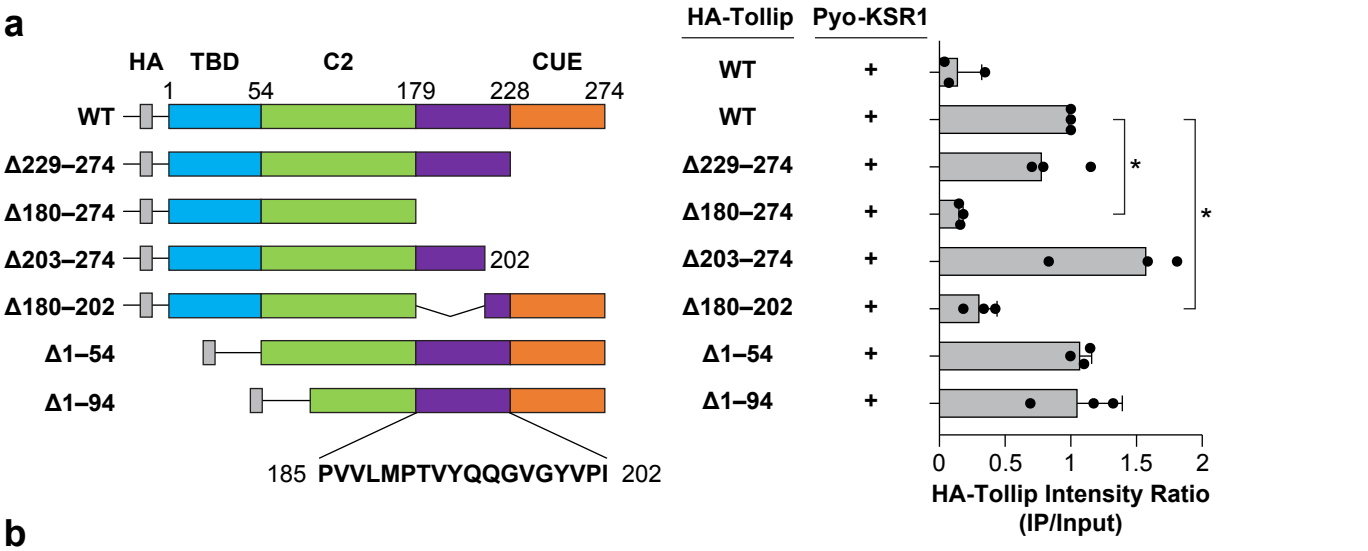

b

```
FRUITFLY–D.lebanonensis   176 EGSIDIVLSYSLQPFTYPIAGTS-------FLVGSNARPIVLTP-------VHQA----- 216
SPIDER–A.ventricosus      175 EGTINLVITCQPIPSGNLIYHPK------SLVTIVPFGPFSDEEGVVSDRPVSHVNDQSR 228
C.elegans                 162 EGMIHLHFSFAPIDLPLQQA---------------------------------------- 181
FROG–X.laevis             139 EGMINLVMSYTSVPA--MMPAQPVVLMPTVYQQGVGYVPIAD--PIYNPGMP-------- 210
ZEBRAFISH                 163 EGMINLVMSFATIPAGMMMQPQPVVLMPTVYQQGVGYVPIAGVPGMYNQGVVPMG----- 193
HUMAN                     163 EGMINLVMSYALLPAAMVMPPQPVVLMPTVYQQGVGYVPITGMPAVCSPGMVPVA----- 217
RAT                       163 EGMINLVMSYTSLPAAMMMPPQPVVLMPTVYQQGVGYVPIAGMPAVCSPGMVPMA----- 217
MOUSE                     163 EGMINLVMSYTSLPAAMMMPPQPVVLMPTVYQQGVGYVPIAGMPAVCSPGMVPMA----- 217
RHESUS-MONKEY             163 EGMINLVMSYTSLPAAMMMPPQPVVLMPTVYQQGVGYVPIAGMPAVCSPGMVPMA----- 217
                                  ** *.: ::          185                 202
```

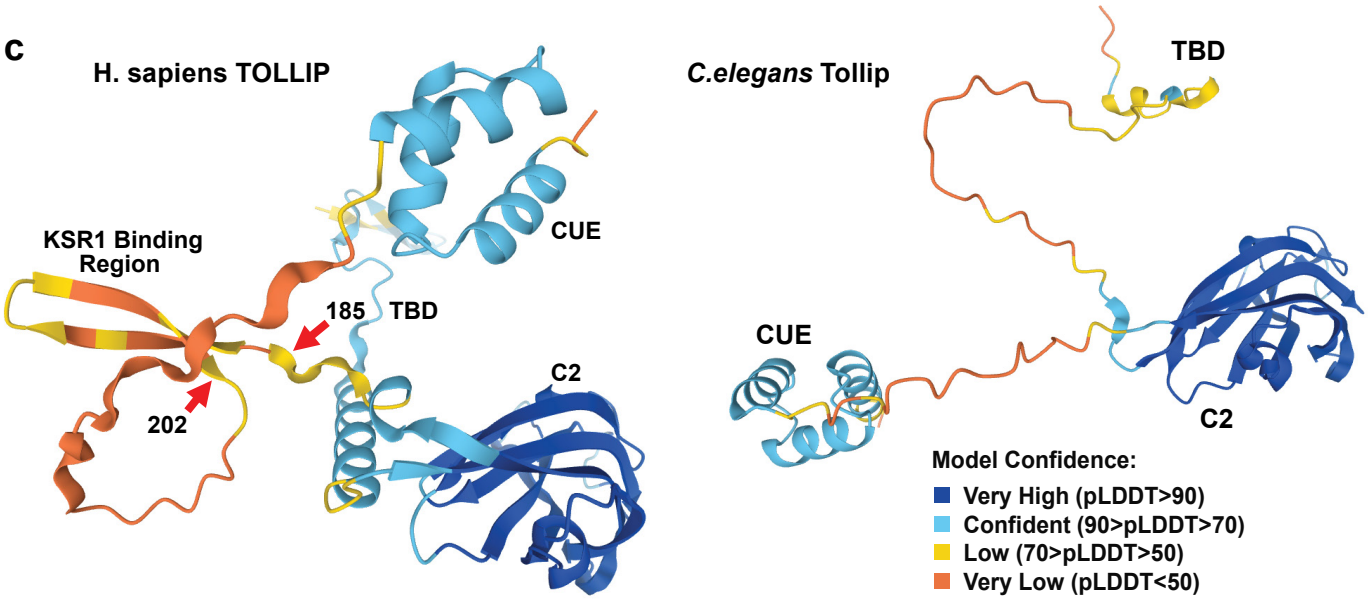

Figure 4

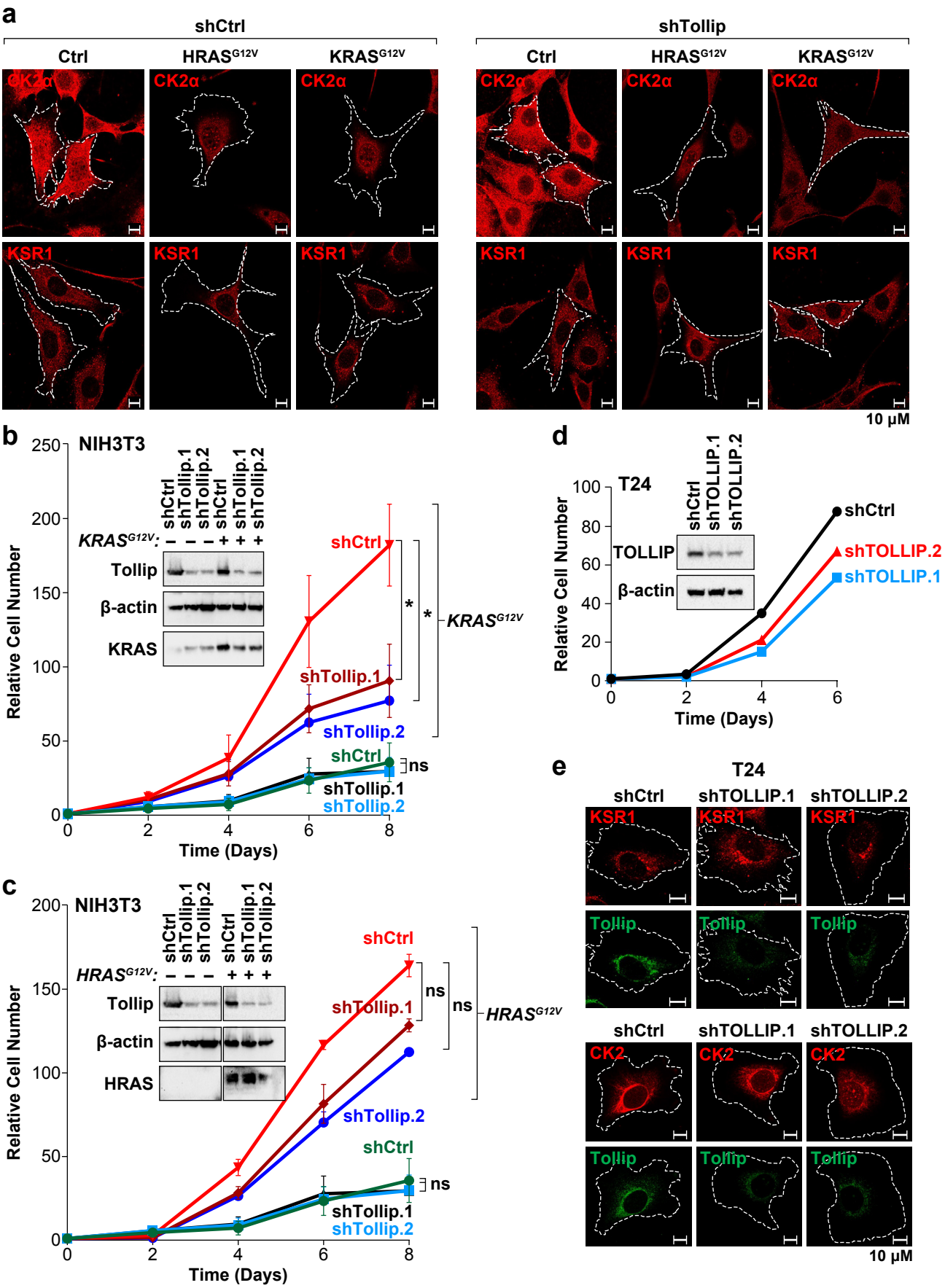

Figure 5

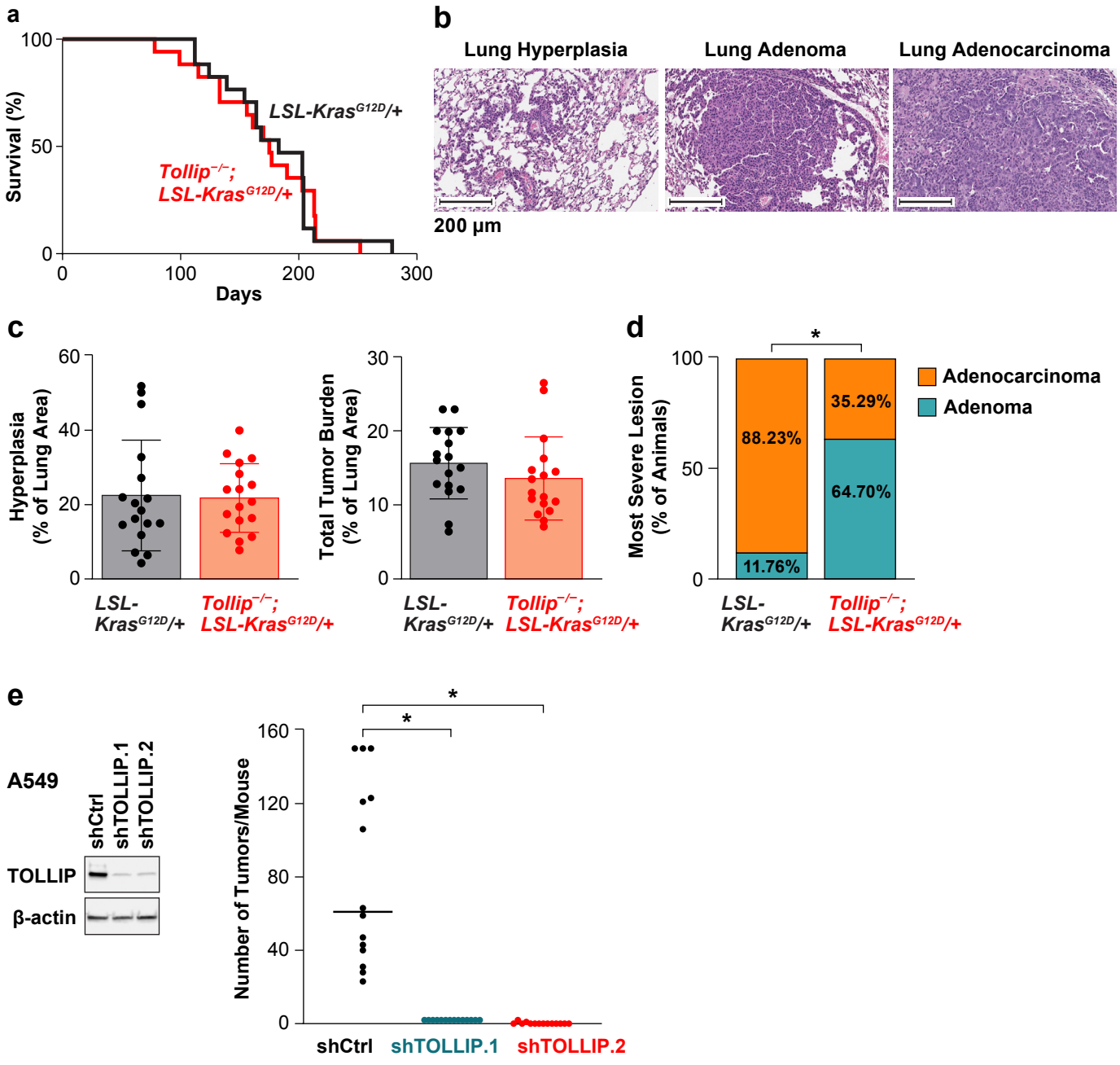

Figure 6

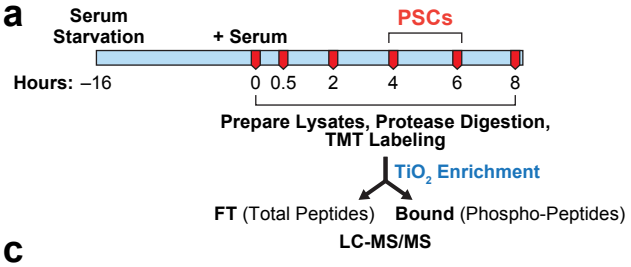

b CK2 Phosphorylation Motif: pS/pT•X•X•D/E

	Total p-Peptides	CK2 p-Peptides	CK2 p-Peptides (%)
All	6091	3252	53.39
4 Hours	76	43	56.5789474
6 Hours	143	82	57.3426573
4+6 Hours	29	16	55.1724138

c CK2 p-Peptides: 4+6 Hours

Protein Name	Annotated Sequence	CK2 Motif	Known CK2 Site
Pdap1	KSLDSDE**S63**EDEDDDYQQK	8–11 SedE	Y
Rplp0	EESEE**S307**DEDMGFGLFD	6–9 SdeD	Y
Nmt1	LPAPSLPLMMEGNGNGHEHC**S31**DCENEEDNSHNR	21–24 SdcE	N
Hnrnpul2	AVEEQGDDQDSEKSKPAG**S191**DGER	19–22 SdgE	N
Eif5b	K**T107**SFDENDSEELEDK	2–5 TsfD	N
8030462N17Rik	**S66**ESETSTMAAK	1–4 SesE	N
Mybbp1a	QLQHGEDED**S722**DNEDNK	10–13 SdnE	N
Sec31a	VDGPDVALKDSDQVAQ**S526**DGEESPAAEEQLLGER	17–20 SdgE	Y
Pdcd4	DSGRGD**S76**VSDNGSEAVR	7–10 SvsD	Y
Dek	EE**S247**SEDEEKESEEEQPPKK	3–6 SseD	Y
Usp15	GASAATGIPLE**S961**DEDSNDNDNDLENENCMHTN	12–15 SdeD	Y
Riok1	MASVVPGQFDDADS**S22**DSENK	15–18 SdsE	Y
Pin4	GGAA**S19**GSDSADK	5–8 SgsD	N
Pbdc1	GAD**S184**GGEKEEGANR	4–7 SggE	N
Cbx3	K**S93**LSDSESDDSK	2–5 SlsD	Y
Eif4b	**T420**GSESSQTGASATSGR	1–4 TgsE	N

d Gene Ontology (MF)

4+6 Hours

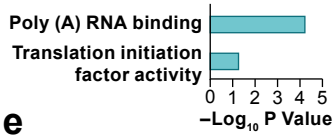

e

4 Hours

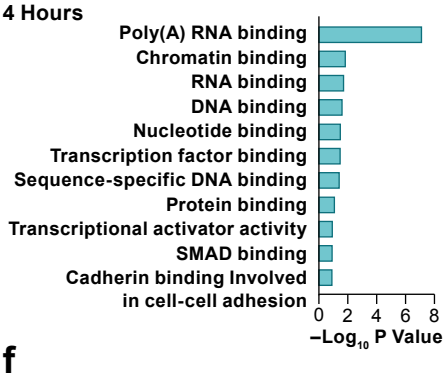

f

6 Hours

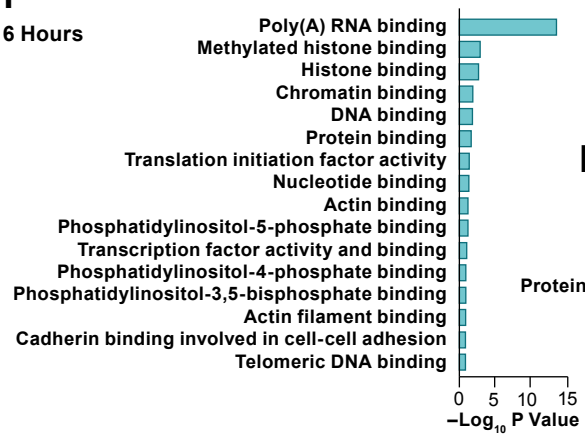

g A549: Tollip-Dependent CK2 p-Peptides

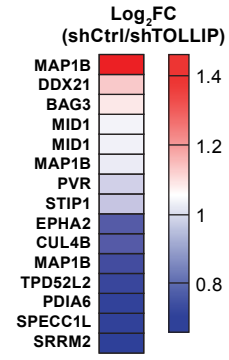

h

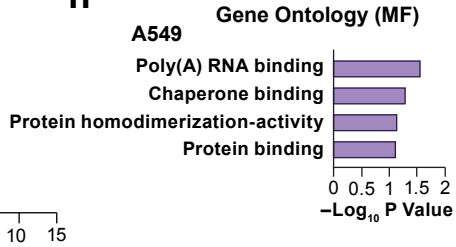

i MEFs: KRAS-Induced, Tollip-Dependent CK2 p-Peptides

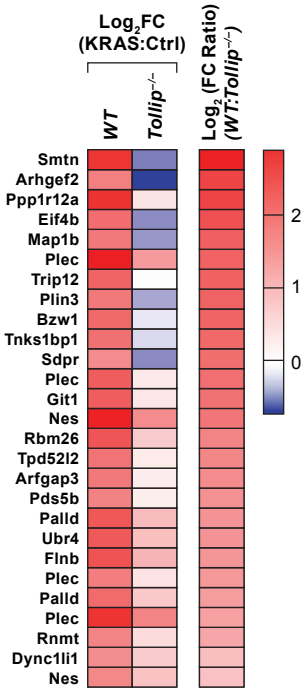

j Gene Ontology (MF)

MEFs

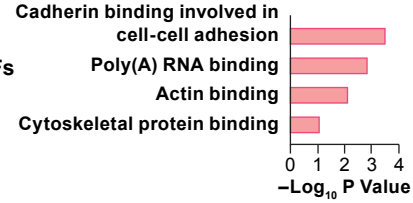

k Common p-Peptides ≥2 Datasets

Protein Name	Annotated Sequence	CK2 Motif
EIF4B	[R].SQS**S**DTEQPSPTSGGGK.[V]	4–7 SdtE
TPD52L2	[R].NSATFK**S**FEDR.[V]	7–10 SfeD

l Common Proteins ≥2 Datasets

EIF4B	UBR4	SRRM2	TPD52L2
MAP1B	TNKS1BP1	SDPR	

Gene Ontology (MF)

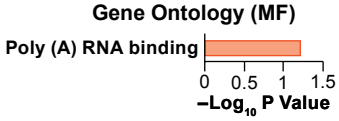

Figure 7